RESEARCH ARTICLE SUMMARY

IMMUNOMETABOLISM

A metabolic dependency of EBV can be targeted to hinder B cell transformation

Bojana Müller-Durovic, Jessica Jäger†, Christine Engelmann†, Patrick Schuhmachers, Sabine Altermatt, Yannick Schlup, Urs Duthaler, Celia Makowiec, Gunhild Unterstab, Sarah Roffeis, Erta Xhafa, Nadine Assmann, Fredrik Trulsson, Rebekah Steiner, Joy Edwards-Hicks, James West, Lorinda Turner, Leyla Develioglu, Robert Ivanek, Tarik Azzi, Philippe Dehio, Christoph Berger, Swiss Transplant Cohort Study, Dmitry Kuzmin, Sophie Saboz, Josef Mautner, Jordan Löliger, Marco Geigges, Darya Palianina, Nina Khanna, Stefan Dirnhofer, Christian Münz‡, Glenn R. Bantug‡, Christoph Hess*

INTRODUCTION: More than 90% of the adult population worldwide are infected with the Epstein-Barr virus (EBV). EBV, which belongs to the γ-herpes virus family, is transferred through saliva, and, if symptomatic, de novo infection causes infectious mononucleosis. The virus is B cell tropic and establishes lifelong latent infection in this cellular compartment. Originally, EBV was identified in Burkitt's lymphoma cells, and the virus is well known for its growth-transforming and tumorigenic properties. EBV can also cause life-threatening hyperinflammation (hemophagocytic lymphohistiocytosis) and has also been strongly associated with the development of autoimmunity (e.g., multiple sclerosis and systemic lupus erythematosus). When infecting B cells, EBV causes their rapid growth and proliferation, a metabolically demanding process that is a prerequisite for establishing latency.

RATIONALE: The metabolic challenge that EBV imposes on nascently infected B cells may create bottlenecks for the virus en route to establishing latent infection. Targeting such early host cell metabolic dependencies of EBV could hinder progression to latency, the infection stage underpinning most EBV-related pathologies.

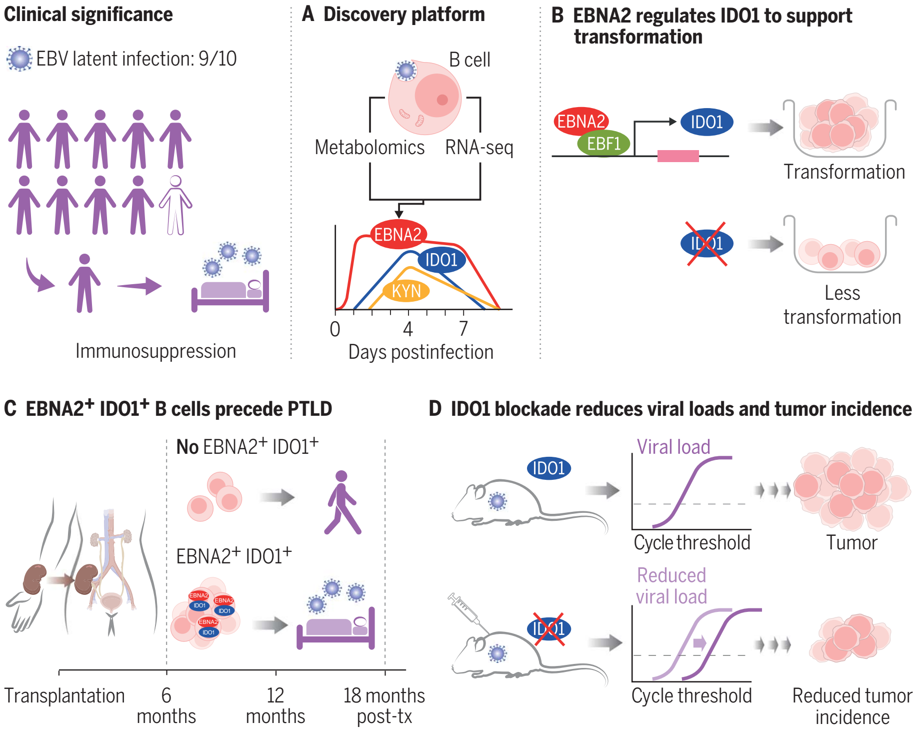

Latent EBV infection depends on IDO1. More than 90% of the adult population are infected with EBV. (**A**) Unbiased analyses identified up-regulation of kynurenine pathway (KP) activity early after EBV infection of B cells. RNA-seq, RNA sequencing. (**B**) EBV-orchestrated induction of the key KP enzyme, IDO1, supported B cell transformation. (**C**) Viral hijacking of KP activity was detected in the blood of transplant patients ahead of lymphoma development. post-tx, posttransplantation. (**D**) Blocking IDO1 reduced viremia and tumor incidence in mice.

RESULTS: We performed unbiased metabolomic and transcriptome-based analyses and found evidence that the activity of the kynurenine pathway and the nicotinamide adenine dinucleotide (NAD) de novo synthesis pathway were up-regulated in B cells during the prelatency phase after EBV infection. We discovered that the viral protein, EBV-encoded transactivator EBNA2, in cooperation with the host B cell transcription factor EBF1, drove induction of indoleamine 2,3-dioxygenase 1 (IDO1), the first and rate-limiting enzyme of the kynurenine pathway. IDO1-dependent degradation of tryptophan fueled NAD de novo synthesis, which supported mitochondrial adenosine triphosphate production in the early phase of EBV infection. Pharmacologic inhibition of IDO1 rendered B cells up to 100-fold less susceptible to EBV transformation, a hurdle that was removed by adding back the product of IDO1, kynurenine, as well as by supplementing nicotinic acid mononucleotide, the direct precursor of NAD.

In the peripheral blood of patients that eventually developed posttransplant lymphoma, we identified a population of B cells that expressed EBNA2 as well as IDO1, suggesting that, before development of EBV-driven malignancy, the molecular axis we uncovered in vitro may be engaged in vivo. In mice, blocking IDO1 pharmacologically, or deleting IDO1 genetically in B cells, reduced EBV viral loads and inhibited the formation of B cell tumors.

CONCLUSION: Early after infecting B cells, EBV induced the expression of IDO1 in host cells, which changed the activity of B cell metabolic pathways. Hijacking this host axis was a metabolic requirement for the virus to efficiently establish latent infection, in vitro and in vivo. Targeting IDO1 clinically may thus offer an opportunity to interfere with progression of EBV infection in B cells from prelatency to latency. EBV-naïve solid organ transplant recipients are at a very high risk for developing posttransplantation lymphoproliferative disorders (PTLDs), particularly when EBV-negative recipients receive tissue from EBV-positive donors. In this context, pharmacological inhibition of IDO1 could limit EBV-driven pathology. Precisely defining metabolic bottlenecks that viruses have evolved to depend upon in vivo may identify druggable targets beyond IDO1 in other settings. ■

The list of author affiliations is available in the full article online.
*Corresponding author. Email: chess@uhbs.ch
†These authors contributed equally to this work.
‡These authors contributed equally to this work.
Cite this article as B. Müller-Durovic *et al.*, *Science* 385, eadk4898 (2024). DOI: 10.1126/science.adk4898

READ THE FULL ARTICLE AT
https://doi.org/10.1126/science.adk4898

RESEARCH ARTICLE

IMMUNOMETABOLISM

A metabolic dependency of EBV can be targeted to hinder B cell transformation

Bojana Müller-Durovic[1]†, Jessica Jäger[1]‡, Christine Engelmann[2]‡, Patrick Schuhmachers[2], Sabine Altermatt[1]§, Yannick Schlup[1], Urs Duthaler[3], Celia Makowiec[1], Gunhild Unterstab[1], Sarah Roffeis[1], Erta Xhafa[1], Nadine Assmann[1,4], Fredrik Trulsson[1], Rebekah Steiner[1]¶, Joy Edwards-Hicks[5], James West[5], Lorinda Turner[5], Leyla Develioglu[1], Robert Ivanek[6], Tarik Azzi[7,8], Philippe Dehio[1], Christoph Berger[7], Swiss Transplant Cohort Study#, Dmitry Kuzmin[9,10], Sophie Saboz[1], Josef Mautner[11], Jordan Löliger[1], Marco Geigges[1], Darya Palianina[12], Nina Khanna[12], Stefan Dirnhofer[13], Christian Münz[2], Glenn R. Bantug[1]**, Christoph Hess[1,5]***

After infection of B cells, Epstein-Barr virus (EBV) engages host pathways that mediate cell proliferation and transformation, contributing to the propensity of the virus to drive immune dysregulation and lymphomagenesis. We found that the EBV protein EBNA2 initiates nicotinamide adenine dinucleotide (NAD) de novo biosynthesis by driving expression of the metabolic enzyme indoleamine 2,3-dioxygenase 1 (IDO1) in infected B cells. Virus-enforced NAD production sustained mitochondrial complex I activity, to match adenosine triphosphate (ATP) production with bioenergetic requirements of proliferation and transformation. In transplant patients, IDO1 expression in EBV-infected B cells, and a serum signature of increased IDO1 activity, preceded development of lymphoma. In humanized mice infected with EBV, IDO1 inhibition reduced both viremia and lymphomagenesis. Virus-orchestrated NAD biosynthesis is therefore a druggable metabolic vulnerability of EBV-driven B cell transformation, opening therapeutic possibilities for EBV-related diseases.

Epstein-Barr virus (EBV) is an oncogenic γ-herpes virus that infects >90% of the adult population worldwide (*1*). Upon infection of B cells, EBV drives a process referred to as transformation, which is characterized by a growth program leading to continuous cell proliferation and establishment of lifelong latency (*2*). During the prelatent phase of infection, the viral master regulator EBNA2 (Epstein-Barr nuclear antigen 2) orchestrates cell activation and cell cycle entry, thereby critically contributing to long-term persistence of the virus (*3*, *4*).

In immunocompetent individuals, primary EBV infection is often oligosymptomatic, or even asymptomatic, when acquired in childhood. Acquisition of EBV during adolescence can result in a febrile illness [glandular fever or infectious mononucleosis (IM)], which usually resolves within weeks. IM is a benign immunopathology characterized by pronounced expansion of inflammatory CD8$^+$ T cells triggered by EBV-infected B cells (*5*). People harboring mutations in immune-related genes can, however, suffer from uncontrolled EBV infection with associated severe immunopathology and a high risk for virus-driven B cell lymphomagenesis (*5*). The pathogenic potential of EBV becomes even more apparent in immunosuppressed patients, for example, after solid organ or allogeneic stem cell transplantation. In these individuals, primary infection may not be controlled or latent infection can reactivate. This may cause a wide spectrum of pathologies, ranging from severe IM-like CD8$^+$ T cell lymphoproliferation to frank lymphoma, such as Burkitt's lymphoma, Hodgkin's lymphoma, or diffuse large B cell lymphoma (*6*). Almost 2% of all human cancers worldwide have been linked to EBV, underscoring the virus's strong oncogenicity (*7*). The viral master regulator EBNA2 activates the expression of a wide range of host and viral genes and plays a critical role in the transformation of EBV-infected B cells. Consistent with the requirement for EBNA2 to transform B cells, EBV lacking EBNA2 is nontransforming, fails to immortalize B cells in vitro (*8*, *9*), and is much less efficient in inducing lymphoma in vivo (*10*).

Several antiviral drugs inhibit EBV lytic infection in vitro, yet no evidence supports their use in IM, and they have no clear value in treating EBV-associated lymphoproliferative diseases (*11*). Monoclonal antibodies have recently demonstrated efficacy in blocking cell entrance of EBV (*12*–*14*), however, no drugs are available that target latency, the process critical for enabling development of EBV-associated malignancies. Depletion of already latently infected B cells with CD20-directed antibodies is a cornerstone in the therapy of most posttransplantation lymphoproliferative disorders (PTLDs), including polymorphic subtypes and monomorphic lymphoma (*15*–*17*)—providing support to strategies aimed at preventing EBV latency.

EBV-driven B cell expansion is a metabolically demanding process. Accordingly, many metabolic pathways are induced in EBV-infected B cells, including mitochondrial respiration [oxidative phosphorylation (OxPhos)] and mitochondrial one-carbon metabolism, glycolysis, and fatty acid and cholesterol synthesis (*18*, *19*). EBV-infected B cells unable to meet the high virally enforced metabolic needs fail to transform and undergo permanent growth arrest (*20*, *21*). Targeting metabolic vulnerabilities of B cells en route to virus-driven transformation may thus offer therapeutic opportunities. Selectively interfering with metabolic pathways that are essential in nascent infected B cells, as opposed to pathways that broadly support cell functions across tissues, seems particularly attractive. With this notion in mind, we set out to characterize early EBV-driven metabolic changes required for latent transformation of B cells.

Results

EBV-infected B cells transiently up-regulate NAD de novo biosynthesis

To monitor the metabolic and transcriptional responses associated with early EBV infection, metabolomic and transcriptomic analyses were performed at 0, 1, and 4 days postinfection (pi). Specifically, naïve B cells (CD27$^-$, IgD$^+$; IgD, immunoglobulin D) were isolated from healthy donors and infected with the EBV prototype strain B95-8 by spinoculation (*22*). Virus was titrated to yield ≥95% infected B cells corresponding to a multiplicity of infection (MOI) of ≅10 (fig. S1A). Heat-inactivated EBV (h.i. EBV) served as a control for non-infection-related activation of B cells through pathogen-associated molecular patterns (PAMPs) and

---

[1]Immunobiology Laboratory, Department of Biomedicine, University of Basel and University Hospital of Basel, Basel, Switzerland. [2]Viral Immunobiology, Institute of Experimental Immunology, University of Zürich, Zürich, Switzerland. [3]Clinical Pharmacology Laboratory, Department of Biomedicine, University of Basel and University Hospital of Basel, Basel, Switzerland. [4]Axolabs GmbH, Kulmbach, Germany. [5]Cambridge Institute of Therapeutic Immunology and Infectious Disease (CITIID), Department of Medicine, University of Cambridge, Cambridge, UK. [6]Bioinformatics Facility, Department of Biomedicine, University Basel and University Hospital of Basel, Basel, Switzerland. [7]Experimental Infectious Diseases and Cancer Research, University Children's Hospital of Zürich, Zürich, Switzerland. [8]Children's Research Center, University Children's Hospital of Zürich, Zürich, Switzerland. [9]Hornet Therapeutics Ltd, London, UK. [10]Department of Medical Oncology, Yale School of Medicine, New Haven, CT, USA. [11]Department of Gene Vectors, Helmholtz Centre Munich, Munich, Germany. [12]Laboratory of Infection Biology, Department of Biomedicine, University Basel and University Hospital of Basel, Basel, Switzerland. [13]Pathology, Institute of Medical Genetics and Pathology, University Hospital Basel, University of Basel, Basel, Switzerland.

***Corresponding author. Email: chess@uhbs.ch**

†Present address: Center of Experimental Rheumatology, Department of Rheumatology, University Hospital and University of Zürich, Zürich, Switzerland.

‡These authors contributed equally to this work.

§Present address: Novartis Institutes for Biomedical Research, Novartis, Basel, Switzerland.

¶Present address: TranslaTUM–Center for Translational Cancer Research, Technical University of Munich, Munich, Germany.

**These authors contributed equally to this work.

#Swiss Transplant Cohort Study (STCS) authors, collaborators, and affiliations are listed at the end of the main text.

was added at the same concentration as infectious B95-8 virus. B cells were then analyzed at 0, 1, and 4 days pi with EBV and at 0, 1, and 4 days poststimulation with h.i. EBV (Fig. 1A). These time points were chosen because they capture distinct modules of prelatent EBV infection: At day 1 pi, extensive transcriptional changes precede phenotypic and functional changes, whereas at day 4 pi, B cells acquire a lymphoblastoid phenotype, are highly activated, and start to rapidly proliferate (hyperproliferative phase), which precedes their transformation (23, 24). We hypothesized that metabolic adaptations of infected B cells within 4 days pi will be critical to enable cell cycle entrance and initiation of hyperproliferation.

Analysis of single metabolite abundance identified quinolinate, a metabolite of tryptophan formed in the kynurenine pathway, as the most differentially altered metabolite, with a 32-fold increase in EBV-infected B cells at day 4 versus day 1 pi relative to B cells exposed to h.i. EBV (Fig. 1B). Along the kynurenine pathway, tryptophan is sequentially catabolized to L-kynurenine and quinolinate, which, in some cells, can be used for nicotinamide adenine dinucleotide (NAD) de novo biosynthesis (Fig. 1C) (25, 26). Tryptophan levels were decreased in EBV-infected B cells at day 4 pi, indicating increased kynurenine pathway activity (Fig. 1B). Reduced NAD^+ (oxidized form of NAD) abundance supported a kynurenine pathway activation model early in EBV-infected B cells to replenish NAD (Fig. 1B). Notably, NAD de novo biosynthesis was not previously described in B cells. Aligning with this idea, transcripts involved in NAD de novo biosynthesis were up-regulated at day 4 pi, in contrast to those contributing to NAD salvage [NAD regeneration from nicotinamide (NAM)] and the Preiss-Handler pathway [NAD generation from nicotinic acid (NA)] (Fig. 1D). Next, we longitudinally quantified abundance of the kynurenine pathway metabolites tryptophan, L-kynurenine, quinolinate, and NAD^+ over the course of 28 days pi, which is when outgrowth of EBV-infected B cells is observed. In parallel, we assessed established lymphoblastoid cell lines (LCLs) to compare early infected and stably transformed B cells. Intracellular tryptophan levels dropped transiently at days 1 and 4 pi yet were restored to preinfection levels on day 7 pi—which suggested accelerated catabolism of tryptophan toward kynurenines (Fig. 1E, top left panel). Correspondingly, L-kynurenine and quinolinate transiently increased in the first 7 days pi, with the peak in L-kynurenine preceding the peak in quinolinate, its downstream metabolite (Fig. 1E, top middle and top right panels, respectively). Indoleamine 2,3-dioxygenase 1 (IDO1) catalyzes the first and rate-limiting step of tryptophan catabolism (Fig. 1C). Being an established measure of IDO1 activity, the L-kynurenine/tryptophan ratio was transiently increased at day 4 pi (Fig. 1E, bottom left panel), as was the quinolinate/tryptophan ratio from days 1 to 7 pi (Fig. 1E, bottom middle panel) (27). NAD^+ steadily increased, reaching a plateau at around day 7 pi (Fig. 1E, bottom right). IDO1 protein abundance accurately mirrored the quinolinate/tryptophan ratio in this early prelatent phase of EBV infection in B cells (Fig. 1F and fig. S8A). Of note, the two other tryptophan degrading enzymes, IDO2 and TDO (tryptophan 2,3-dioxygenase), were not induced (figs. S1B and S8F).

To test the hypothesis that EBV-infected B cells engage in NAD de novo biosynthesis, isotope tracer studies using uniformly labeled tryptophan (U-^{13}C-tryptophan) were performed (Fig. 1G). Culturing EBV-infected B cells in presence of U-^{13}C-tryptophan from day 0 pi resulted in incorporation of tryptophan-derived heavy carbon atoms into L-kynurenine and quinolinate between days 4 and 7 pi, after which incorporation was no longer detected, further supporting the hypothesis of transient kynurenine pathway activation in B cells early after infection (Fig. 1H). Tryptophan-derived carbons also contributed to both the total cellular NAD^+ and NADH pools (Fig. 1I). To define the contribution of tryptophan-derived carbons to the NAD pool in the absence of NAD salvage, influx via the salvage pathway was blocked using FK866, a specific inhibitor of the enzyme nicotinamide phosphoribosyltransferase (NAMPT) (fig. S1C). Under these conditions, up to 64% of the total NAD pool contained tryptophan-derived carbons (Fig. 1J). Highlighting the importance of this major contribution to de novo NAD biosynthesis in nascent EBV-infected B cells, blocking IDO1 with the selective small-molecule IDO1 inhibitor linrodostat (hereafter, Lin.; BMS-986205, competitor for binding of heme to the apoenzyme) (28) from day 0 pi onward, prevented expansion of the NAD pool (Fig. 1K). Adding Lin. on day 4 pi, by contrast, had no effect on NAD levels, whereas addition of FK866 reduced NAD abundance (Fig. 1K). This indicated that NAD de novo biosynthesis was selectively important early after infection of B cells, and NAD recycling by NAMPT was key for maintaining the expanded pool. Indeed, NAMPT was rapidly up-regulated upon infection of B cells with EBV (fig. S1D).

Together, these data identified transient activation of the kynurenine pathway in nascent EBV-infected B cells. Kynurenine pathway activity was marked by accelerated consumption of tryptophan during early postinfection, resulting in a temporary increase in L-kynurenine and quinolinate that supported NAD de novo biosynthesis. NAD de novo biosynthesis was critically fueling the B cell NAD pool during the first few days of infection.

IDO1 activity is required for transformation of EBV-infected B cells

Next, we aimed to investigate how IDO1 activity and kynurenine pathway–driven NAD de novo biosynthesis related to transformation of newly EBV-infected B cells. In addition to Lin., the competitive IDO1 inhibitor epacadostat (hereafter, Epa.), which binds to heme-free holo-IDO1, and KHK2455, a compound that binds the apoenzyme, were used to block IDO1, thus exploring a range of clinically tested, safe, and selective inhibitors with differing modes of action (29–32). Metabolic tracing with U-^{13}C-tryptophan was performed to ascertain that these drugs also inhibited IDO1 in our system (fig. S2A). Inhibition of IDO1 using Lin., added at the time of infection, was highly effective in suppressing transformation of B cells by EBV (Fig. 2A), while not affecting cell viability (fig. S2B, left panel; this figure also shows titration data on Epa. and KHK2455). To pinpoint whether IDO1 per se, or downstream metabolites of the enzyme, were required for transformation of B cells, metabolite add-back experiments were performed. Addition of L-kynurenine at the time of infection rescued EBV's capacity to transform IDO1-inhibited B cells (Fig. 2A), an effect that was dose dependent (fig. S2C). Uptake of L-kynurenine, and its metabolism toward quinolinate and, to a lesser extent, NAD, were dose dependent as well (fig. S2D). The direct precursor of NAD, nicotinic acid mononucleotide (NaMN), was equally efficient in rescuing EBV-driven B cell transformation (Fig. 2A). Epa. and KHK2455 phenocopied the findings made with Lin. (fig. S2, E and F). Furthermore, small interfering RNA (siRNA)–mediated reduction of IDO1 in EBV-infected B cells also suppressed transformation (Fig. 2B and figs. S2G and S8G).

The transient nature of tryptophan catabolism in B cells recently infected with EBV (Fig. 1, E, F, H, and I) led us to explore the relation between IDO1-driven kynurenine pathway activity and EBV-mediated B cell transformation in a time-resolved manner. When delaying addition of Lin. until day 4 or 8 pi, the drug lost its suppressive effect on EBV's capacity to transform B cells (Fig. 2C). We next added or removed Lin. in 24-hour intervals between day 0 and day 6 pi and measured EBV-driven cell proliferation as a proxy for transformation. In the first 2 days pi, Lin. was sufficient and necessary to reduce the number of proliferating cells, yet it lost its effect at later time points (Fig. 2D). In line with these Lin. add-in and wash-out experiments, NaMN rescued proliferation in IDO1-inhibited EBV-infected B cells only when added in the first 2 days pi (fig. S2H). Cell cycle transition from G1 to S phase has been described as a critical barrier to EBV-mediated B cell transformation (20, 21, 33). In line with this literature, Lin. arrested EBV-infected B cells at G0 to G1 in a manner that

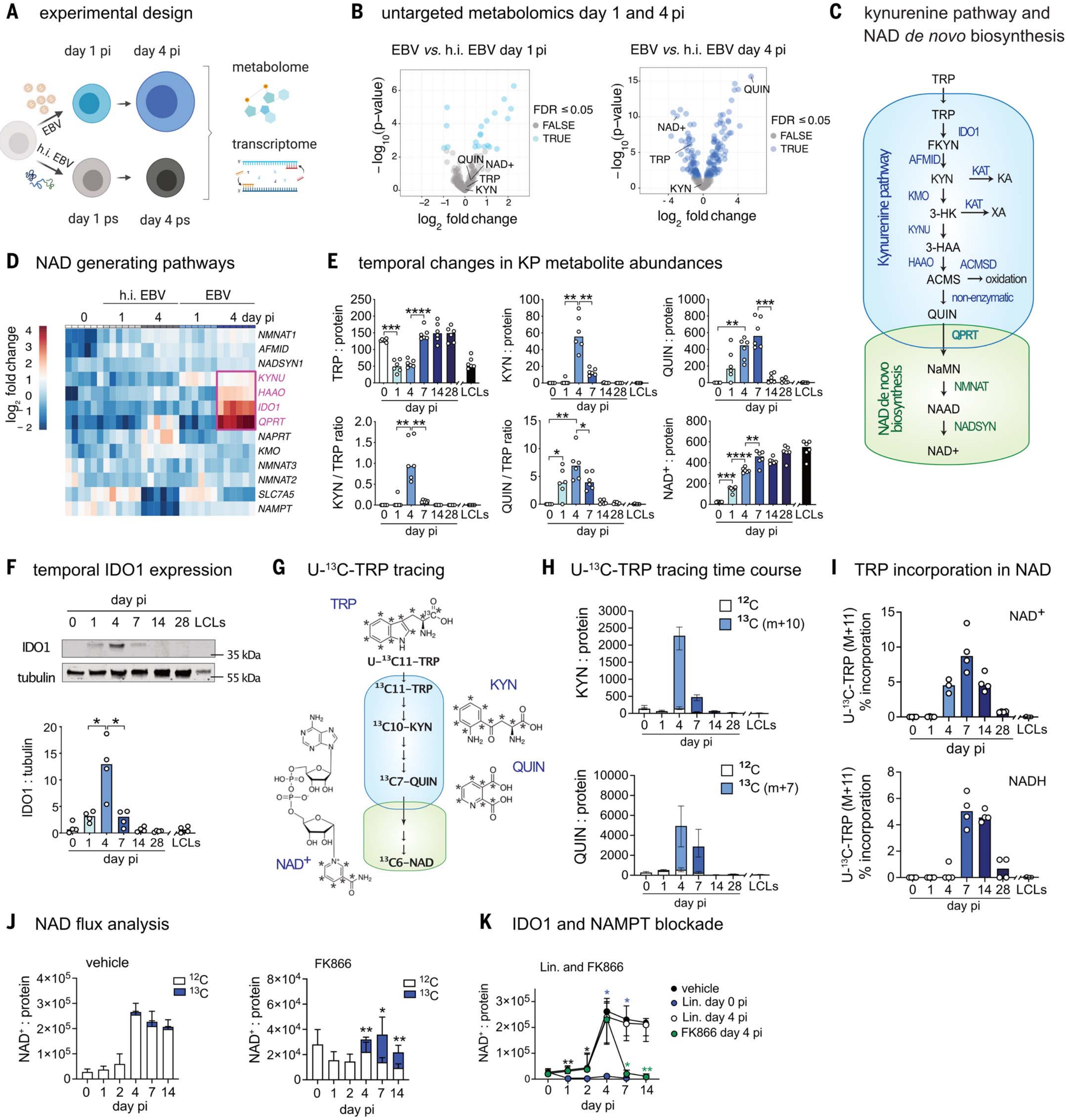

Fig. 1. Metabolic profiling of EBV-infected B cells reveals transient up-regulation of NAD de novo biosynthesis in newly infected B cells. (**A**) Experimental design of metabolome and transcriptome analyses in naïve B cells infected with EBV or stimulated with h.i. EBV; $n = 6$ biologically independent samples, paired analysis. (**B**) Comparison of metabolite abundances between EBV-infected and h.i. EBV–exposed naïve B cells, 1 and 4 days pi (left and right panels, respectively). Colored dots indicate significantly changed metabolites (FDR ≤ 0.05). Metabolites linked to NAD de novo biosynthesis are labeled: nicotinamide adenine dinucleotide (NAD), tryptophan (TRP), L-kynurenine (KYN), and quinolinate (QUIN). (**C**) Scheme of the kynurenine pathway and interlinked NAD de novo biosynthetic pathway. AFMID, arylformamidase; ACMSD, aminocarboxymuconate semialdehyde decarboxylase; HAAO, 3-hydroxyanthranilate 3,4-dioxygenase; KAT, kynurenine aminotransferase; KMO, kynurenine 3-monooxygenase; KYNU, kynureninase; NADSYN, NAD synthetase; NMNAT, nicotinamide nucleotide adenylyltransferase; QPRT, quinolinate phosphoribosyltransferase; ACMS, aminocarboxymuconate semialdehyde; FKYN, formyl-L-kynurenine; 3-HAA, 3-hydroxyanthranilic acid; 3-HK, 3-hydroxykynurenine; KA, kynurenic acid; XA, xanthurenic acid. (**D**) Hierarchical clustering of transcripts involved in NAD metabolism in EBV-infected naïve B cells and naïve B cells stimulated with h.i. EBV at days 0, 1, and 4 pi. Up-regulated transcripts involved in NAD de novo biosynthesis are highlighted and shown as $\log_2$ fold change to the average expression of the respective gene within the dataset. (**E**) Metabolite abundance of TRP, KYN, QUIN, and ratios of KYN/TRP and QUIN/TRP,

as well as NAD$^+$ in bulk B cells, before and at five time points after infection, as indicated, and compared with LCLs. Data are represented as mean values of indicated individual data points ($n = 6$ independent experiments). (**F**) Representative immunoblot (top panel) and pooled data from $n = 4$ independent experiments (bottom panel) of IDO1 expression in bulk B cells, before and at five time points after infection, as indicated, and compared with LCLs. Data are shown as median values of indicated individual data points. (**G**) Schematic of tracer incorporation into the kynurenine pathway and interlinked NAD de novo biosynthetic pathway using U-^{13}C-TRP. (**H**) Fraction of ^{13}C-labeled KYN (m+10) (upper panel) and QUIN (m+7) (lower panel) at indicated time points after infection of bulk B cells, and in LCLs, normalized to total protein. Data are shown as median values and range, $n = 4$ independent experiments. (**I**) U-^{13}C-TRP incorporation into total cellular NAD$^+$ (top panel) and NADH (bottom panel). Data are shown as median values of indicated individual data points ($n = 4$ independent experiments). (**J**) U-^{13}C-TRP incorporation into total cellular NAD$^+$ after blockade of NAD recycling with FK866 (added at day 0 pi) (right panel) and with vehicle control (left panel) displayed as medians. (**K**) Total NAD$^+$ levels, as assessed by mass spectrometry in EBV-infected bulk B cells before and at five time points after infection as indicated, treated with vehicle, Lin. added at day 0 pi, Lin. added at day 4 pi, and FK866 added at day 4 pi. Data are shown as median of four independent experiments, comparing vehicle and Lin. day 4 pi (black stars), vehicle and Lin. day 0 pi (blue stars), and vehicle and FK866 day 4 pi. Experiments (A), (B), and (D) were performed using naïve B cells, experiments (E) to (K) were performed using bulk B cells. Data in (E) and (F) were compared using a repeated measures ANOVA test followed by multiple comparisons test; data in (J) and (K) were compared using a one-way ANOVA followed by multiple comparisons test. P values are indicated as: $*P \leq 0.05$, $**P \leq 0.001$, $***P \leq 0.0001$, $****P \leq 0.00001$.

was rescued by L-kynurenine and NaMN (Fig. 2E and fig. S2I). These findings were recapitulated with KHK2455 in conjuncture with NaMN add-back (fig. S2J). IDO1 thus functions as a metabolic checkpoint governing cell cycle entrance in early EBV-infected B cells.

Given that NAD de novo biosynthesis, fueled by IDO1, was a prerequisite for proliferation and transformation of EBV-infected B cells, we next aimed to define how this metabolic axis was regulated. IDO1 is an interferon (IFN)–responsive gene with cell-intrinsic antiviral properties described for several viral infections (*34*–*36*). To test whether IDO1 was induced in early EBV-infected B cells through an IFN response, Janus kinase (JAK) signaling was blocked using tofacitinib. IFNγ-stimulated noninfected B cells were tested in parallel. Tofacitinib abrogated IDO1 expression in IFNγ-stimulated noninfected B cells, whereas expression of IDO1 in EBV-infected B cells was largely insensitive to JAK inhibition (fig. S2K). These data argued against induction of IDO1 reflecting primarily an antiviral response of EBV-infected B cells.

Early after infection, EBNA2, a key viral transactivating factor in the prelatent phase of infection (*37*), showed temporal coexpression with IDO1 in EBV-infected B cells at protein (Fig. 2F and fig. S8B) and mRNA levels (fig. S2L). This association was lost in LCLs, where EBNA2 was expressed, whereas IDO1 remained undetectable (Fig. 2F)—likely because the *IDO1* promotor was methylated beyond day 8 pi (fig. S2M). We thus reasoned that EBNA2 could be involved in regulating IDO1 specifically in the first few days after infection. To test this idea, B cells were infected with either wild-type (WT) EBV (B95-8) or an EBNA2-deleted EBV strain (P3HR1). IDO1 was only induced by WT and not EBNA2-deleted EBV (Fig. 2G and fig. S8C). EBNA2 deficiency also regulates expression of other viral transcription factors, with many downstream effects (*3*). Therefore, to examine a potential direct link between EBNA2 and expression of IDO1, chromatin immunoprecipitation–polymerase chain reaction (ChIP-PCR) experiments were performed. In these assays, EBNA2 was identified to associate with *IDO1* DNA in B cells infected with B95.8 and not in P3HR1-infected cells (Fig. 2H), with methylenetetrahydrofolate dehydrogenase 2 (MTHFD2) serving as positive control (fig. S2N) (*18*). To probe whether EBNA2 was sufficient to induce expression of IDO1, a B cell line constitutively expressing an estrogen receptor hormone binding domain–EBNA2 fusion protein (ER-EBNA2) was used (DG75$^{\text{ER-EBNA2}}$ cell line) (*38*). In this system, estrogen drives cytoplasmic-to-nuclear translocation of the ER-EBNA2 complex. Because the *IDO1* promoter is methylated in these cells (fig. S2O), the effect of estrogen on expression of *IDO1* was probed both in presence and absence of the demethylation agent 5-aza-2′-deoxycytidine (5-azadC). In both the methylated and demethylated setting, addition of estrogen mediated a clear increase in *IDO1* expression (Fig. 2I). Expression of EBNA2 in DG75$^{\text{ER-EBNA2}}$ cells was modest (fig. S2P), and estrogen itself had no effect on IDO1 expression in the parental cell line (fig. S2Q), excluding artificially high EBNA2 levels and estrogen as confounders. Direct lentiviral overexpression of EBNA2 in Ramos cells, a lymphoblastoid EBV-negative B cell line, was likewise sufficient to induce IDO1 (Fig. 2J). Together these data established that EBNA2 regulated expression of IDO1 in vitro.

To test whether EBNA2 also regulated expression of IDO1 in B cells in vivo, NOD-scid γc$^{-/-}$ (NSG) mice were adoptively transferred with B cells infected with either WT EBV (B95-8) or the EBNA2-deleted strain P3HR1. On day 7 after transfer, EBV-positive IDO1-expressing B cells (EBNA1$^+$ IDO1$^+$) were abundant both in the spleen and peripheral blood of mice transferred with WT infected B cells (Fig. 2K). By contrast, no IDO1 was detected in B cells infected with EBNA2-deleted EBV (Fig. 2K), establishing that EBNA2 was also required in vivo to drive expression of IDO1 in EBV-infected B cells.

We used a humanized mouse model of EBV infection to assess whether EBNA2$^+$ IDO1$^+$ B cells were detected in this preclinical model of natural EBV infection. Briefly, NSG mice were injected with human hematopoietic progenitor and stem cells shortly after birth, and reconstitution with human immune system components was confirmed at 3 to 4 months of age by flow cytometry (fig. S3A). Humanized mice were subsequently infected with a high dose of EBV (10^5 infectious units), and emergence of EBNA2$^+$ IDO1$^+$ B cells was monitored weekly in peripheral blood and in the spleen at week 5 pi—the legal end point of this experiment. In line with the data derived from adoptive transfer of B cells infected with EBNA-competent versus EBNA-deleted EBV (Fig. 2K), in WT EBV-infected mice, IDO1-expressing EBV-infected B cells (EBNA2$^+$ IDO1$^+$) were readily detected both in peripheral blood and the spleen (Fig. 2L).

EBNA2 does not bind DNA directly but rather requires a cellular factor to initiate transcription (*39*). We therefore aimed to define the host DNA binding element enabling EBNA2-driven *IDO1* transcription. EBNA2 ChIP–Re-ChIP experiments identified early B cell factor 1 (EBF1), rather than the prominent EBNA2 binding factor CBF1 (*18*, *37*, *38*), to interact with IDO1 DNA (Fig. 2M). Indeed, a highly stable structure of this complex binding to DNA is predicted by AlphaFold2 (fig. S3C and movie S1). Confirming the functional relevance of EBF1 as a EBNA2-hijacked host transcription factor, CRISPR-Cas9–mediated editing of EBF1 in primary B cells infected with EBV imposed a corresponding decrease in IDO1 expression (Fig. 2N).

We next tested whether induction of IDO1 is a common feature of B cell proliferation. To that end, B cells were either infected with EBV B95-8 or stimulated with CpG, anti- CD40L&IL-4 (IL-4, interleukin-4), or IL-21. Proliferation and expression of IDO1 was monitored on days 0, 2, 4, and 7 poststimulation or postinfection. In EBV-infected B cells, peak IDO1 expression coincided with initiation of proliferation, around day 4 pi, whereas IDO1 was not induced by other proliferation-triggering stimuli (figs. S2R and S9). Induction of IDO1 was thus restricted to early WT EBV infection and not a common trait of B cell proliferation.

Together, these data demonstrated that EBNA2, through EBF1, regulated IDO1 in nascent EBV-infected B cells. To explore how in

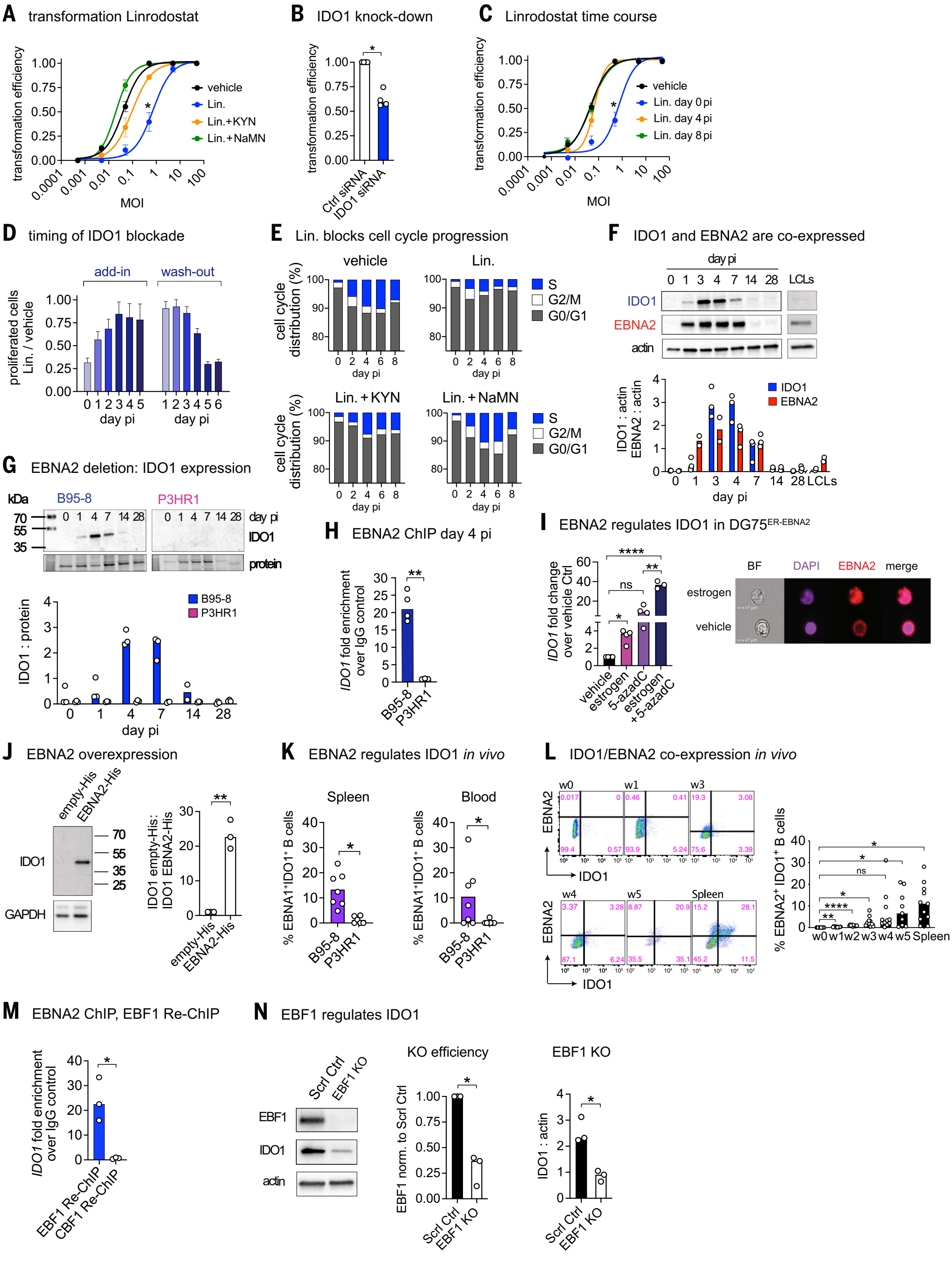

Fig. 2. EBNA2-regulated IDO1 activity underpins EBV's capacity to transform B cells. (**A**) EBV-mediated B cell transformation efficiency was quantified in presence of 10 μM Lin., Lin. with 100 μM KYN, or Lin. with 500 μM NaMN and compared with vehicle control. The percentage of wells with cell outgrowth at week 5 pi was plotted against the MOI of B95-8 EBV ± SD, *n* = 3 or 4 independent experiments. Sigmoidal curve fitting, confidence interval (CI) = 95%. (**B**) EBV-mediated B cell transformation efficiency (at an MOI of 1) was quantified after siRNA-mediated knockdown of IDO1 at day 1 pi and compared with scrambled siRNA treatment (Ctrl siRNA). Data are represented as median value of indicated individual data points (*n* = 4 independent experiments) relative to Ctrl siRNA (set at one). (**C**) EBV-mediated B cell transformation efficiency at week 5 pi after addition of 10 μM Lin. as a single dose on day 0, 4, or 8 pi. (**D**) Ratio of the number of B cells proliferating at day 8 pi in presence versus absence of IDO1 inhibition with Lin. Add-in (left panel): Lin. was added in 24 hours intervals to EBV-infected B cells from day 0 to day 6 pi. Wash-out (right panel): Lin. was added on day 0 pi to EBV-infected bulk B cells and washed away in 24-hour intervals. Data are shown as median ± 95% CI, *n* = 3 independent experiments. The gating strategy is shown in fig. S10A. (**E**) Cell cycle status of EBV-infected B cells treated with vehicle, 10 μM Lin., 10 μM Lin. and 100 μM KYN, and 10 μM Lin. and 500 μM NaMN, as indicated. Reagents were added at the time of infection as a single dose. Data are shown as median values from *n* = 4 independent experiments. The gating strategy is shown in fig. S10B. (**F**) Protein abundance of IDO1, EBNA2, and actin (loading control) in B cells at the indicated time points after infection and in LCLs. Representative immunoblot (top panel) and summary data quantified from *n* = 2 or 3 independent experiments shown as median of indicated individual data points (IDO1 and EBNA2 protein abundance, normalized to actin) (bottom panel). (**G**) IDO1 protein abundance in B cells infected with B95-8 EBV or the EBNA2-deleted EBV strain, P3HR1, at the indicated time points after infection. Representative immunoblot (top panel) and summary data quantified from *n* = 3 independent experiments shown as median of indicated data points (IDO1 protein abundance, normalized to total protein) (bottom panel). (**H**) EBNA2 ChIP-qPCR analysis of *IDO1* in B cells infected with EBV B95-8 or EBV P3HR1 at day 4 pi. Bars depict median fold enrichment of *IDO1* EBNA2 ChIP signal over *IDO1* signal from the IgG control ChIP, and individual data points from *n* = 4 independent experiments are shown. (**I**) *IDO1* mRNA abundance in DG75$^{ER\text{-}EBNA2}$ cells (shown relative to vehicle control, set to one) treated with estrogen, the demethylating agent 5-azadC, or estrogen and 5-azadC. Median fold increase and individual data points from *n* = 3 or 4 independent experiments are shown (left panel). Representative image stream

pictures assessing nuclear translocation of the ER-EBNA2 complex in DG75 cells in response to estrogen as compared with vehicle control (right panel). (**J**) Representative immunoblot of IDO1 abundance in Ramos cells transduced to overexpress EBNA2 (EBNA2-His) or an empty control lentivirus (empty-His). Glyceraldehyde phosphate dehydrogenase (GAPDH) was used as a loading control. Summary data from three independent experiments are shown as fold increase in IDO1 expression in EBNA2-His–transduced compared with empty His-transduced cells. (**K**) Frequency of EBNA$^+$ IDO1$^+$ B cells in mice infected with WT B95-8 versus EBNA2-deleted P3HR1 EBV strain as assessed by flow cytometry in splenic B cells (left panel) and peripheral blood B cells (right panel), both at day 7 pi. Data are shown as mean of indicated individual data points. The gating strategy is shown in fig. S10C. (**L**) IDO1 and EBNA2 coexpression was monitored longitudinally in peripheral blood B cells of humanized mice infected with EBV B95-8 by flow cytometry. At week 5 pi, splenic B cells were also analyzed. The left panel shows representative staining from one mouse (upper right quadrant = EBNA2$^+$ IDO1$^+$ B cells, parent population CD19$^+$ cells). The right panel shows cumulative data from 11 mice analyzed using the gating strategy indicated on the left. The gating strategy is shown in fig. S10C. (**M**) qPCR analysis of *IDO1* from EBNA2 ChIP followed by Re-ChIP with EBF1 and Re-Chip with CBF1. Median fold changes over IgG control ChIP from $n = 3$ independent experiments are shown. (**N**) EBF1 abundance in bulk B cells after CRISPR-Cas9–mediated editing of *EBF1* or treatment with scrambled gRNA (left panel: representative immunoblot; middle panel: summary data from $n = 3$ independent experiments). IDO1 protein abundance was quantified in KO and control B cells 4 days after EBV infection (right panel). Experiments (A) to (H), (M), and (N) were performed using human bulk B cells. Data in (B), (H), (J), (K), (M), and (N) were compared using a two-tailed Student's *t* test; data in (I) and (L) were compared using a repeated measures ANOVA test followed by Tukey's multiple comparisons test. *P* values are indicated as: $^*P \leq 0.05$, $^{**}P \leq 0.001$, $^{***}P \leq 0.0001$, $^{****}P \leq 0.00001$.

nascent EBV-infected B cells the EBNA2/EBF1 axis might regulate gene expression beyond IDO1, EBNA2 ChIP–EBF1 Re-ChIP sequencing experiments were performed. By doing so, EBNA2/EBF1 target genes of other key metabolic pathways, such as OxPhos, fatty acid metabolism, and DNA repair, were identified—highlighting the broad impact EBV has on basic host cell functions (fig. S3D).

The IDO1–NAD axis enables mitochondrial ATP production to match demand

Our next goal was to define how IDO1-driven NAD de novo biosynthesis related to the metabolic reprogramming required to enable EBV-driven B cell proliferation and transformation. Analysis of the transcriptome of B cells at days 1 and 4 pi revealed prominent up-regulation of OxPhos-related genes, which preceded induction of glycolysis-related transcripts (Fig. 3A and table S1). Aligning with these RNA sequencing (RNA-seq) data, OxPhos activity assessed by metabolic flux analysis also increased ahead of glycolysis (Fig. 3B and fig. S4, A and B). Of note, this rapid increase in OxPhos, and the interlinked shift of the OxPhos/glycolysis ratio, was not observed in cells exposed to h.i. EBV (fig. S4, A and B). Furthermore, induction of OxPhos was also only observed in B cells infected with EBNA2-competent virus, and it was suppressed by inhibition of IDO1 (fig. S4C). Together these data pointed at EBNA2- and IDO1-dependent early mitochondrial respiration being a hallmark of EBV-enforced B cell metabolic reprogramming.

To assess at the molecular metabolic level how IDO1 activity and NAD de novo biosynthesis contributed to the prominent mitochondrial respiration observed early after EBV infection of B cells, we performed metabolic flux experiments. Inhibiting IDO1 with Lin. prevented up-regulation of OxPhos at day 2 pi, and this phenotype was reverted by addition of L-kynurenine or NaMN (Fig. 3C). Overexpression of IDO1 in LCLs increased OxPhos (Fig. 3D). NAD de novo biosynthesis, fueled by IDO1, was thus required for induction of mitochondrial respiration in early EBV-infected B cells, and expressing IDO1 in LCLs was sufficient to increase OxPhos. Differentiating the contribution of mitochondrial respiration versus glycolysis to adenosine triphosphate (ATP) production in EBV-infected B cells revealed that earlier than day 4 pi, most ATP was derived from mitochondrial respiration, with a switch to glycolysis as the main ATP source at around 4 days pi (Fig. 3E).

Further linking the IDO1–NAD axis to bioenergetics, ATP cellular abundance was reduced in response to IDO1 blockade, resulting in an increased cellular adenosine diphosphate (ADP)/ATP ratio (Fig. 3F). Add-back of the IDO1-fueled metabolites, L-kynurenine and NaMN, reverted the ADP/ATP ratio (Fig. 3F). IDO1–NAD dependent cellular ATP was mitochondria-derived, as evidenced by metabolic flux experiments in presence of Lin. with or without L-kynurenine or NaMN (Fig. 3G). In addition to establishing the need of IDO1-fueled NAD for sufficient mitochondrial ATP production, these experiments also indicated that glycolysis was unable to compensate for the acute bioenergetic (i.e., ATP) deficit imposed by blocking IDO1 (Fig. 3G). By contrast, at approximately day 4 pi, aerobic glycolysis provided most of the cellular ATP (Fig. 3E), thus rendering IDO1–NAD–dependent mitochondrial ATP less limiting.

NADH delivers electrons to Q10 of the respiratory chain at complex I. Therefore we tested individual activity of the respiratory complexes I, II, and IV in EBV-infected B cells after IDO1 inhibition with Lin. In conjunction with NaMN add-back, these experiments established that IDO1, by fueling NAD production, specifically increased activity of complex I (Fig. 3H and fig. S4D). The relevance of complex I activity, specifically, early in the process of EBV-driven B cell transformation was underscored using a complex I–blocking compound, rotenone, at low concentrations. When present in transformation assays at the time of infection, rotenone potently inhibited outgrowth (i.e., latent infection) of transformed B cells, an effect that was lost when adding the inhibitor at day 8 pi (Fig. 3I). This pattern of dependency on fully functional complex I aligned with the reliance of EBV-infected B cells on OxPhos for ATP synthesis specifically in the first few days after infection (Fig. 3E). The importance of the IDO1–NAD axis to OxPhos was also reflected at the ultrastructural level: Mitochondrial abundance was reduced in EBV-infected B cells cultured in the presence of the IDO1 inhibitor Lin., a deficit corrected by addition of L-kynurenine or NaMN (fig. S4E, left panel). Further, while IDO1 inhibition did not alter the length/width ratio of mitochondria (fig. S4E, middle left panel), it was associated with rupture of the double membrane, irregularities in cristae organization, and swollen dense mitochondria—ultrastructural abnormalities that were corrected by addition of L-kynurenine as well as NaMN (fig. S4E, middle right and right panels). These experiments established the requirement for EBV-orchestrated NAD de novo biosynthesis to ensure mitochondrial bioenergetic sufficiency early during B cell transformation.

To test whether the effects of Lin., and hence IDO1 activity, were specific to EBV-infected B cells, we evaluated the impact of the inhibitor on B cells stimulated with h.i. EBV, CpG, and B cell receptor (BCR) cross-linking (Fig. 3J). RNA-seq identified 158 differentially expressed genes between B cells infected with EBV in presence versus absence of Lin. (fig. S5A). These transcriptional changes were not recapitulated when activating B cells with h.i. EBV, CpG, or BCR ± Lin., indicating that Lin. had specific effects on the transcriptome of EBV-infected B cells (Fig. 3J). Additionally, activation of B cells [as assessed by expression of CD69 and human leukocyte antigen–DR isotype (HLA-DR)], cell apoptosis, and B cell differentiation (defined by IgD and CD27) (40) were not affected by Lin. in noninfected B cells; B cells infected with EBV; or B cells stimulated with h.i. EBV, CpG, BCR–cross-linking, or anti-CD40L&IL4 and IL-21 (fig. S5, B and C). Only CD38, which is expressed on recently EBV-activated B cells (23, 41), was less abundant selectively on Lin.-treated EBV-infected B cells, aligning with

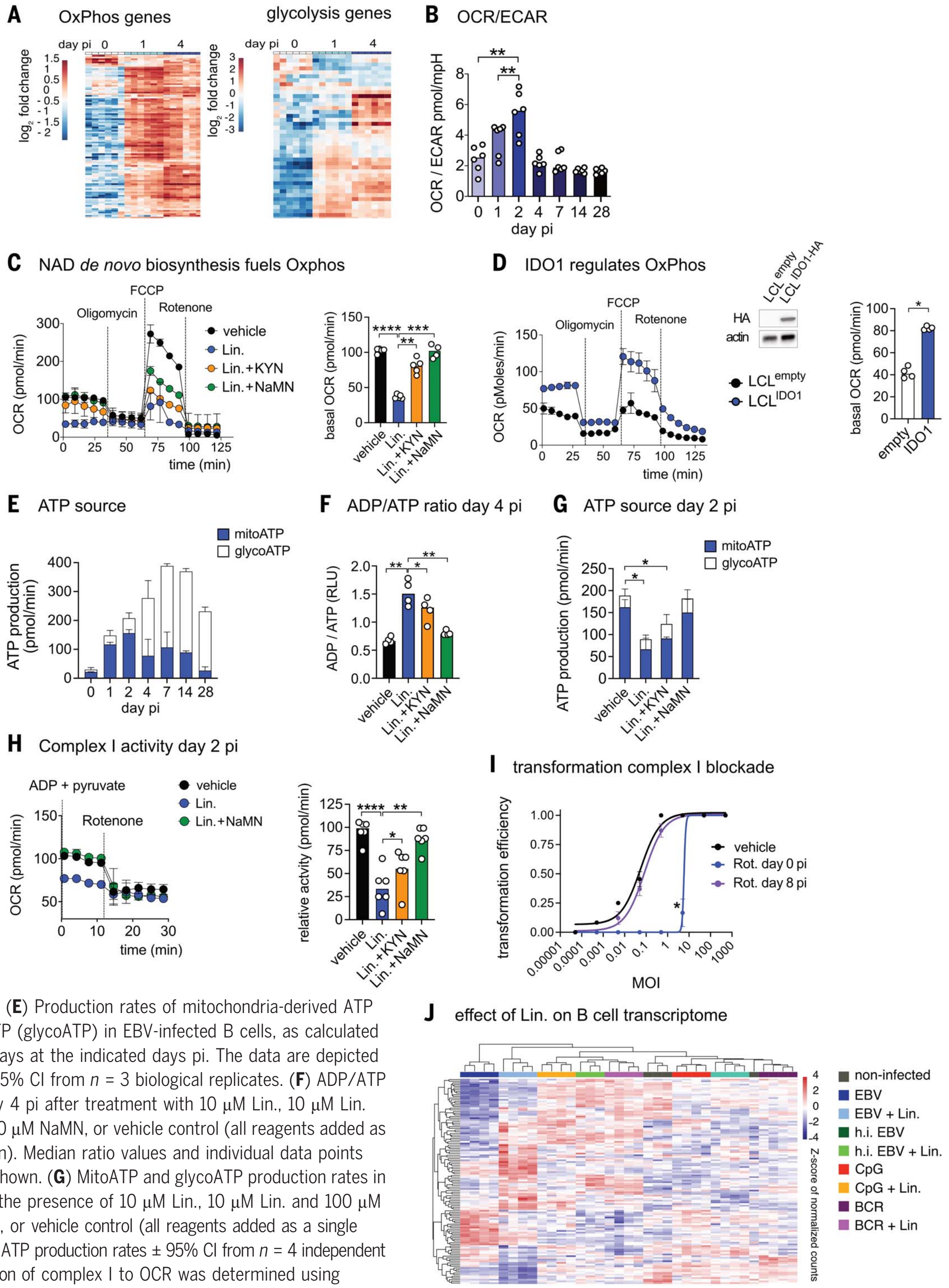

Fig. 3. IDO1-enabled NAD de novo biosynthesis supports mitochondrial respiration and interlinked ATP production. (**A**) Hierarchical clustering of transcript abundance from genes involved in OxPhos and glycolysis in EBV-infected naïve B cells on days 0, 1, and 4 pi shown as $\log_2$ fold change to the average expression of the respective gene within the dataset. (**B**) OCR/ECAR ratios as assessed by metabolic flux analyses in EBV-infected bulk B cells at the indicated time points pi. Mean values of pooled data and individual data points from $n = 3$ biological replicates are shown. (**C**) Mitochondrial perturbation of EBV-infected bulk B cells at day 4 pi treated with vehicle control, 10 μM Lin., 10 μM Lin. and 100 μM KYN, and 10 μM Lin. and 500 μM NaMN (all reagents were added at the time of infection). A representative OCR perturbation profile (left panel) and median basal OCR values and individual data points (right panel) from $n = 4$ or 5 biological replicates are shown. (**D**) OCR profiles of LCLs transfected to overexpress IDO1 versus transfection with an empty control plasmid (left panel). Representative immunoblot, probing IDO1 protein abundance in LCLs transfected with IDO1 containing versus empty vector (middle panel). Median basal OCR values of pooled data and individual data points from $n = 4$ biological replicates are shown. (**E**) Production rates of mitochondria-derived ATP (mitoATP) and glycolysis-derived ATP (glycoATP) in EBV-infected B cells, as calculated from mitochondrial perturbation assays at the indicated days pi. The data are depicted as median ATP production rates ± 95% CI from $n = 3$ biological replicates. (**F**) ADP/ATP ratios in EBV-infected B cells on day 4 pi after treatment with 10 μM Lin., 10 μM Lin. and 100 μM KYN, 10 μM Lin. and 500 μM NaMN, or vehicle control (all reagents added as a single dose at the time of infection). Median ratio values and individual data points from $n = 4$ biological replicates are shown. (**G**) MitoATP and glycoATP production rates in EBV-infected B cells at day 2 pi, in the presence of 10 μM Lin., 10 μM Lin. and 100 μM KYN, 10 μM Lin. and 500 μM NaMN, or vehicle control (all reagents added as a single dose at the time of infection). Median ATP production rates ± 95% CI from $n = 4$ independent experiments are shown. (**H**) Contribution of complex I to OCR was determined using metabolic flux analyses after permeabilization of cells and addition of ADP and pyruvate followed by rotenone (1.3 μM). The left panel shows a representative OCR profile at day 4 pi of vehicle-treated cells, cells treated with Lin. 10 μM, and cells treated with Lin. 10 μM and NaMN 500 μM. The right panel depicts mean values from $n = 6$ biological replicates. (**I**) EBV-mediated bulk B cell transformation efficiency was quantified in the presence of rotenone (1.3 μM) added at day 0 pi and at day 8 pi, as a single dose each, or vehicle control. The percentage of wells with cell outgrowth at week 5 pi was plotted against the MOI of B95-8 EBV ± SD, $n = 2$ independent experiments. Sigmoidal curve fitting was performed, CI = 95%. (**J**) Hierarchical clustering of B cells infected with EBV or stimulated with h.i. EBV, CpG, or BCR cross-linking, with or without Lin. (2 days for all conditions). Clustering was performed on the basis of genes differentially expressed 2 days pi in EBV-infected B cells treated with Lin. compared with EBV-infected B cells without Lin. (fig. S4F). Read counts were normalized by variance-stabilizing transformation and Z-scored. Data in (B), (C), and (E) to (H) were compared using a repeated measures one-way ANOVA test followed by Tukey's multiple comparisons test. Data in (D) were compared using two-tailed Student's *t* test. *P* values are indicated as: *$P \le 0.05$, **$P \le 0.001$, ***$P \le 0.0001$, ****$P \le 0.00001$.

the drug's impact on establishing latency (fig. S5, B and C).

These data established a key impact of IDO1 blockade specifically manifesting in the context of EBNA2/EBF1-orchestrated induction of the enzyme. Blocking IDO1 reduced OxPhos by hindering complex I activity, secondary to insufficient NAD de novo biosynthesis.

EBV-induced IDO1 activity in B cells underpins viral pathology in vivo

To explore the in vivo relevance of EBV-driven IDO1 activity for the development of pathologies related to latent B cell infection, we took advantage of the prospective Swiss Transplant Cohort Study (STCS) ([42](42)). The STCS is a large collaboration, clinically monitoring and biosampling all solid organ transplant (SOT) recipients in Switzerland. From this cohort, 10 patients were identified with histologically confirmed EBV-associated PTLD, diagnosed 6 to 18 months posttransplantation. Tumor biopsy samples from 7 of these 10 cases were available and independently reassessed and verified to be EBV-positive PTLDs by EBV-encoded small RNA (EBER) immunohistochemistry (fig. S6A, left panel). Expression of IDO1 in EBV-positive (i.e., EBER$^+$) B cells was observed in all latency types (fig. S6A, right panel). Of note, 3 of 10 transplant recipients that developed PTLD were EBV seronegative at the time of transplantation and received an organ from an EBV-seropositive donor (table S2). Control patients with no evidence of PTLD (n = 20) were matched with cases for age, sex, transplanted organ, and creatinine levels and stratified into two groups: (i) participants with no viral syndrome and no documented EBV reactivation within 18 months posttransplantation (no EBV react., n = 10), and (ii) patients with ≥1 detectable EBV DNA sample within the 6- to 18-month posttransplantation observation period (EBV react., n = 10). Clinical details of these transplant patients are provided in table S2. For all study participants, serum and peripheral blood mononuclear cell (PBMC) samples were available pretransplant (t0) and at 6 months (t6) and 12 months (t12) posttransplantation.

Using cytometry by time of flight (CyTOF) technology, we assessed how IDO1 was expressed in B cells, monocytes (CD14$^+$), and dendritic cells (CD11c$^+$) in all study participants longitudinally (Fig. 4A). Because our focus was on understanding the pathophysiology of latency development, that is, the premalignant phase of EBV-driven B cell tumors, only pre-PTLD samples were characterized. In patients who went on to develop PTLD, expression of IDO1 increased in B cells at t12 as compared with t6 and t0 (Fig. 4A, top panel). Future PTLD patients further expressed more IDO1 in CD14$^+$ monocytes than patients without PTLD, with no apparent temporal dynamics (Fig. 4A, middle panel). IDO1 expression among dendritic cells was similar in all three groups (Fig. 4A, bottom panel). Visualizing expression of IDO1 and EBNA2 in B cells that were clustered according to expression of IgD, CD27, CD21, CD20, IgM, CD23, EBNA1, EBNA2, and LMP1 (latent membrane protein 1) revealed a distinct population of EBNA2$^+$ IDO1$^+$ B cells emerging in future PTLD patients (Fig. 4B). Expression of IDO1, EBNA2, and LMP1 in EBV-positive B cells did not correlate between tumor tissues and matched peripheral blood B cells (fig. S6B), suggesting that the circulating EBNA2$^+$ IDO1$^+$ B cells detected pre-PTLD diagnosis and tumor cells were distinct cellular entities. Next, serum abundance of tryptophan, L-kynurenine, and quinolinate was analyzed by mass spectrometry in this same cohort. Tryptophan levels were lower and serum L-kynurenine and quinolinate levels overall increased in pre-PTLD samples as compared with samples from both control groups, pointing at increased tryptophan consumption preceding lymphoma diagnosis (Fig. 4C). The quinolinate/tryptophan ratio—indicative of kynurenine pathway activation—was higher in pre-PTLD samples as compared with control samples (Fig. 4C, bottom right panel). EBV-seronegative PTLD patients did not differ from EBV-seropositive counterparts in these measurements. Aligning with these pairwise comparisons, sensitivity and specificity of "CD19$^+$ IDO1$^+$ EBNA2$^+$ peripheral blood B cells" in predicting or excluding future PTLD was excellent and, when combined with "serum quinolinate/tryptophan ratios," near-perfect (Fig. 4D). Circulating EBNA2$^+$ IDO1$^+$ B cells and activation of the kynurenine pathway thus preceded EBV-driven PTLD—providing associative evidence for a role of EBV-driven IDO1 activity in lymphomagenesis in SOT recipients.

To investigate the role of IDO1 in acute EBV infection and lymphomagenesis directly, humanized NSG mice were used as described above (Fig. 2L and fig. S3A). Details of experimental modalities applied to individual cohorts of EBV-infected mice are summarized in Fig. 4E. In the first cohort, intraperitoneal Epa. or vehicle control treatment was initiated three days before infecting mice and maintained for 2 weeks pi. This regimen reduced the tumor incidence quantified at 5 weeks pi (Fig. 4F, left panel), as well as blood and spleen viral loads (Fig. 4F, middle left and middle panel). All tumors, from Epa. and vehicle-treated mice alike, were EBV-positive (EBER$^+$) and EBNA2-positive (fig. S6C, representative examples). Expansion of CD8$^+$ T cells correlated with viral loads in the mouse model used ([43–45](43)) and is a hallmark of EBV infection ([46](46)). Epa. treatment reduced peripheral blood CD8$^+$ to CD4$^+$ T cell ratios (Fig. 4F, middle right panel), secondary to reduced CD8$^+$ T cell expansion (Fig. 4F, right panel, and fig. S5D)—indicative of reduced viral load with IDO1 inhibition. Of note, a limitation of this preclinical model is that human T cells are selected in the context of mouse major histocompatibility complex (MHC) and thus do not fully recapitulate human immune responses. However, the phenotype of CD8$^+$ T cells expanding in EBV-infected mice resembles the phenotype of expanded CD8$^+$ T cells in IM ([47](47)). Furthermore, CD4$^+$ as well as CD8$^+$ T cell clones isolated after EBV-driven T cell expansion in humanized mice recognize autologous LCLs ([48](48)).

Next, we compared antiviral efficacy of 2 versus 5 weeks of IDO1-blockade in a back-to-back setting, switching to oral (drinking water) administration of the drug (Fig. 4E, experimental scheme). Both regimens were successful in reducing tumor incidence and viral loads, with the 5-week treatment being somewhat superior (Fig. 4G). No differences in tumor control, or impact on viremia, were observed between Epa. and KHK2455 (fig. S6E). The therapeutic window of IDO1 blockade was then tested by delaying initiation of IDO1 blockade to weeks 2 pi (Fig. 4E). IDO1 blockade initiated in mice with an already established infection failed to alter the course of infection or disease (fig. S6F). Together, these experiments established that early administration of organismal IDO1 blockade reduced EBV-driven lymphomagenesis and viral loads.

To disentangle systemic effects of IDO1 inhibition from B cell–intrinsic IDO1 blockade, we used a gene knockout (KO) approach. Specifically, IDO1 KO and WT (control-treated) B cells were infected with EBV (B95-8) and transferred into NSG mice. Viral loads were monitored weekly, and tumors enumerated and weighed 4 weeks pi (the legal end point) (Fig. 4H). B cell IDO1 KO was sufficient to reduce tumor incidence, tumor weight, and viral loads (Fig. 4I). These data confirmed B cell–intrinsic IDO1 as a metabolic target of EBV-driven lymphomagenesis, in alignment with our cellular, molecular, and molecular-metabolic findings (Figs. 1 to 3).

Lastly, we aimed to determine whether the IDO1-blocking drug Epa. had additional effects on T or B cells. Epa. did not affect CD8$^+$ or CD4$^+$ T cells numbers in noninfected humanized mice (fig. S7A), and in vivo T cell activation through CD3 cross-linking was not altered by Epa. in C57BL/6 mice (fig. S7B). Epa. also did not affect in vitro expansion of EBV-specific cytotoxic T lymphocytes (CTLs) and did not alter their memory phenotype, activation (expression of CD69), or function [production of IFNγ or tumor necrosis factor (TNF), up-regulation of CD107 (degranulation), expression of granzyme B] (fig. S7, C and D). Administration of Epa. in EBV-infected and noninfected humanized mice also did not change B cell numbers or frequencies (fig. S7E, left panels), B cell activation (expression of CD23, CD39, and CD70) ([23](23), [49](49)) (fig. S7E, top right panels), or B cell memory phenotypes as defined by expression of IgD and CD27 (fig. S7E, bottom right panels).

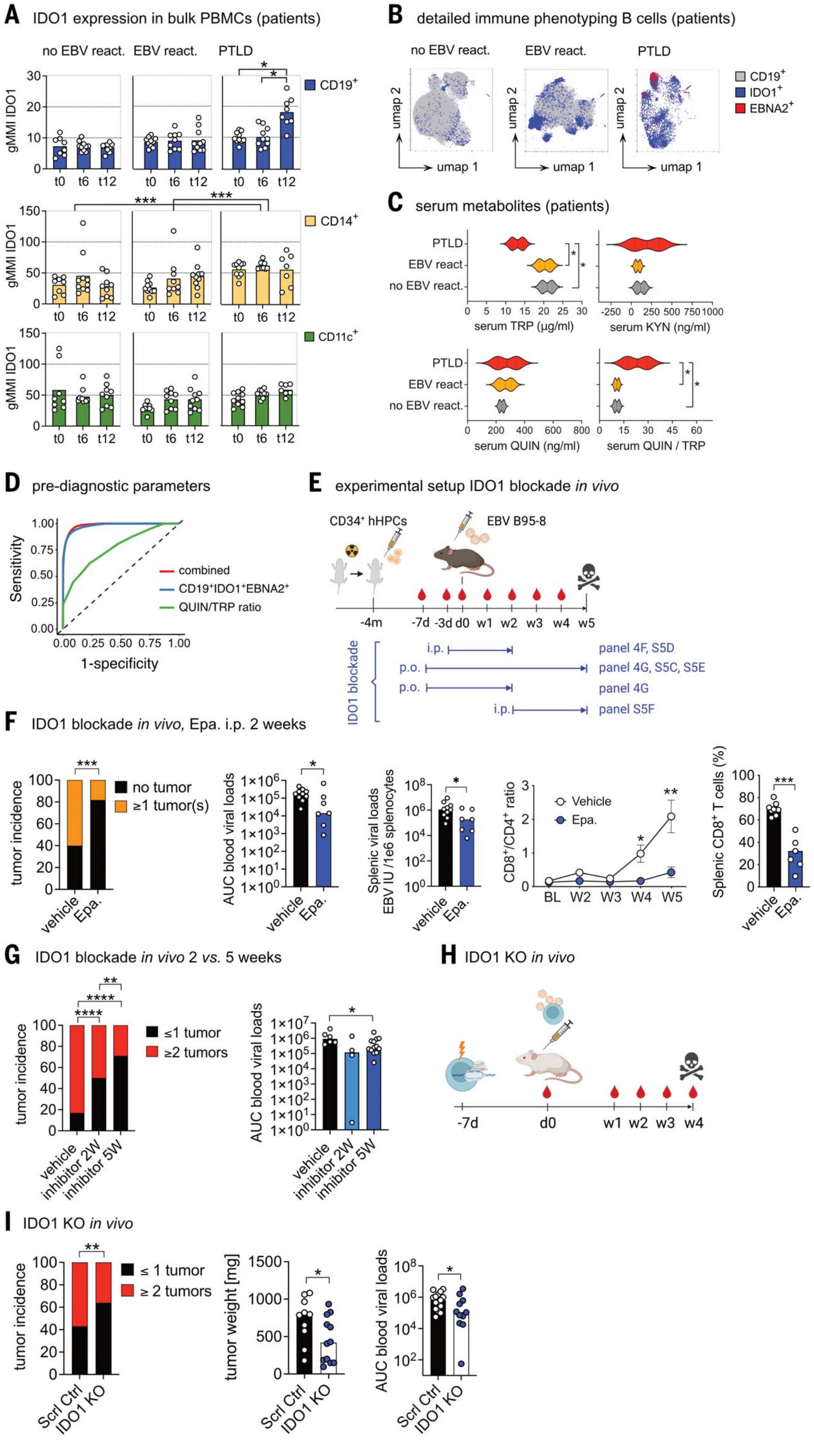

Fig. 4. EBV-induced IDO1 activity in B cells contributes to immune dysregulation and tumorigenesis in vivo. (**A**) IDO1 expression was assessed by CyTOF technology in $CD19^+$ B cells, $CD14^+$ monocytes, and $CD11c^+$ dendritic cells from SOT recipients grouped as follows: (i) without EBV reactivation (no EBV, *n* = 10); (ii) with EBV PCR positivity on at least one occasion in the first 18 months after transplantation (EBV, *n* = 10); (iii) with biopsy-confirmed EBV-positive posttransplantation lymphoproliferative disorder (PTLD, *n* = 10), before (t0) and 6 and 12 months after transplantation (t6 and t12). Data are shown as geometric mean metal intensities (gMMIs). (**B**) Uniform manifold approximation and projection (UMAP) plots derived from CyTOF phenotyping data of $CD19^+$ peripheral blood B cells. For the PTLD group, only pre-PTLD diagnosis samples were included. (**C**) Posttransplant serum TRP, KYN, and QUIN concentrations and posttransplant QUIN/TRP ratios. For the PTLD group, only pre-PTLD diagnosis samples were included. The violin plots indicate median ± IQR and range. (**D**) ROC assessment of the frequency of $EBER^+$ $IDO1^+$ B cells and the serum QUIN/TRP ratio, as well as these two measures combined, in PTLD patients versus patients with EBV reactivation. (**E**) Experimental design of IDO1 blockade in a humanized mouse model of EBV infection and summary of cohorts assessed. (**F**) Tumor incidence 5 weeks pi, in humanized mice treated with Epa. intraperitoneally for 2 weeks pi (*n* = 7) or vehicle control (*n* = 10), shown as no tumor (black) and ≥1 tumor(s) (orange) (left panel); viral loads in blood [area under the curve (AUC) from 2 to 5 weeks pi (middle left panel)]; splenic viral loads at week 5 pi (middle panel); CD8/CD4 T cell ratio in peripheral blood from base line (BL) to week 5 pi (middle right panel) (the gating strategy is provided in fig. S3A); and number of splenic $CD8^+$ T cells (right panel). Data are shown as median values from the indicated individual measurements. (**G**) Tumor incidence in vehicle-treated EBV-infected humanized mice (*n* = 6) and mice treated with IDO1 inhibitor for 2 weeks pi (*n* = 4) and 5 weeks pi (*n* = 12), respectively, shown as ≤1 tumor (black) and ≥2 tumors (red) (left panel). Viral loads from the corresponding experiments are shown as AUC of viral loads from 2 to 5 weeks pi (right panel). Data are shown as median values from the indicated individual measurements. (**H**) Experimental design of adoptive transfer and EBV infection experiment. (**I**) NSG mice were adoptively transferred with primary human B cells, either IDO KO (*n* = 12 mice) or WT (scrambled control cells; *n* = 10 mice). Tumor incidence was determined 4 weeks pi (left panel); tumor weights (middle panel); viral loads (AUC of viral loads from week 1 to 4 pi) (right panel). Data are shown as median values from the indicated individual measurements. Data in (A) and (C) were compared using repeated measures ANOVA test and one-way ANOVA test, respectively, followed by multiple comparisons test. Tumor incidences in (F), (G), and (I) were compared using a chi-square test. Blood viral loads (G) were compared by one-way ANOVA test and multiple comparisons test. *P* values are indicated as: $^*P \leq 0.05$, $^{**}P \leq 0.001$, $^{***}P \leq 0.0001$, $^{****}P \leq 0.0001$.

In vivo inhibition of IDO1, aimed at hindering development of latent infection, thus emerged as an immunometabolic intervention able to reduce lymphomagenesis driven by this virus.

Discussion

Strategies preventing EBV from establishing latent infection and transforming B cells—viral features underlying most EBV-related pathologies—remain elusive. In this study, we used a time-resolved systems biology approach to explore molecular immunometabolic underpinnings enabling EBV latency. Three key findings were made: (i) EBV drives IDO1 activity through EBNA2/EBF1, which fuels NAD de novo biosynthesis in nascent EBV-infected B cells; (ii) NAD de novo biosynthesis is required to increase OxPhos, which in turn supports B cell proliferation and transformation; and (iii) kynurenine pathway activation and IDO1 expression in EBV-infected B cells precedes development of EBV-associated lymphoma in SOT recipients, and inhibiting IDO1 in EBV-infected humanized mice suppresses viremia, prevents expansion of CD8$^+$ T cells, and reduces development of B cell lymphoma.

Studies on IDO1 in immune cells have largely focused on its role as an IFNγ-responsive gene product causing tryptophan depletion and generation of immune-regulatory kynurenines, thereby inhibiting inflammatory T cell responses (*50*–*52*). IDO1 activity has not been described to fuel NAD de novo biosynthesis in either T or B cells. In macrophages, by contrast, NAD de novo biosynthesis has recently been reported (*25*). Although regulated cell-autonomously in these cells, their metabolic phenotype is similar to the one enforced by EBV through induction of IDO1 in B cells, as, in both settings, NAD de novo production supports mitochondrial respiration by means of complex I. IDO1-dependent NAD de novo generation is thought to be switched on in macrophages as NAD salvage pathways are insufficient to sustain normal cell function (*25*). In nascent infected B cells, EBV thus seems to abuse a “reserve” metabolic pathway by engaging the transcription factor EBF1 through EBNA2 to drive transcription of *IDO1*. This virally enforced, de novo–generated NAD supported mitochondrial ATP production, which was a requirement for cell cycle progression and downstream transformation. Notably, in cancer cells, formate, derived from degradation of tryptophan by IDO1, serves as a one-carbon donor for purine nucleotide biosynthesis (*53*), and one-carbon metabolism and purine biosynthesis were previously shown to play a key role in EBV-driven B cell transformation (*18*). Comparing IDO1 blockade with other metabolic interventions in terms of effect on establishing latency and interlinked downstream pathology, such as targeting one-carbon metabolism or nucleotide biosynthesis, will thus be interesting.

The literature on IDO1-dependent tryptophan metabolism in (non-EBV-related) cancer, as well as its impact on immune regulation and immunotherapy, is extensive [reviewed in (*54*)]. Depleting tryptophan and increasing kynurenines in malignant tissues establishes an immunosuppressive tumor microenvironment. Whether EBV-driven IDO1 activity negatively affects antiviral T cell immunity through this mechanism remains to be tested. Notably, several trials using IDO1 inhibitors in non-EBV-related cancers have returned disappointing results [reviewed in (*55*)]—pointing to a complex role of IDO1 in shaping the immune microenvironment. However, these failed clinical studies established a good clinical safety profile of organismal IDO1 blockade (*55*). If IDO1 inhibitors are to be tested in other clinical settings, for example, with the goal of preventing PTLD, careful safety monitoring, and in particular immune monitoring, will be important. From our own preclinical data reported here, no signal of altered immune reactivity emerged that would preclude clinical testing of IDO1 blockade in the context of the enzyme’s identified role early during EBV infection. Such clinical development efforts should additionally encompass careful natural history studies to prospectively test the value of EBNA2$^+$ IDO1$^+$ B cells and serum evidence of IDO1 activity (quinolinate/tryptophan ratio) as biomarkers predictive of PTLD. The drivers of organismal tryptophan depletion and accumulation of kynurenine and quinolinate in pre-PTLD sera will also require further investigation, as this pattern likely reflects a complex composite end point driven by several factors, including hepatic and renal dysfunction, immune activation and inflammation, and viral replication.

Our finding of EBV-orchestrated IDO1 activity being required cell-intrinsically for outgrowth of B cells points at a precisely instructed potential role for IDO1 inhibitors. Several clinical settings in particular lend themselves to translational investigations: EBV-negative SOT recipients are at a very high risk for developing EBV-driven clinical disease, including PTLD, in particular when receiving an organ from an EBV-positive donor (*11*, *56*). PTLD among these patients almost exclusively derives from the recipient’s B cells, and infection happens through the transplant. In this clinical setting, the time point of infection is thus well defined. Initiating IDO1 inhibition just before transplantation and maintaining the treatment in the first months after transplantation will thus offer a clear proof-of-concept setting to explore the value of blocking IDO1 activity. Our data obtained in SOT recipients that later developed EBV-driven PTLD demonstrate the presence of a population of EBNA2$^+$/IDO1$^+$ B cells. Screening for the appearance of this cell population and initiating IDO1 blockade upon their detection reflects a second rational strategy to test how blocking IDO1 affects outcome. By contrast, in established PTLD, regulation and pathogenic relevance of IDO1 remains unclear, and no rationale for using IDO1 inhibition in this setting can be derived from our work. Lastly, in patients with IM, lytic replication and viral shedding persist for a prolonged period of time (*5*). IDO1 blockade in this context plausibly reduces the spread of infection to further B cells. This may affect acute disease as well as the total pool of EBV-infected B cells. The latter could reduce the risk for downstream development of autoimmune diseases thought to relate to EBV infection and thus maintenance of autoreactive B cells (*57*).

In summary, our data identify IDO1 activity and interlinked NAD de novo biosynthesis as a key metabolic requirement—and druggable dependency—of EBV en route to driving B cell transformation. IDO1 blockade emerges as the first precision medicine cellular-metabolic intervention that affects viral infection in vivo—offering potential therapeutic opportunities for a broad range of EBV-associated diseases.

Materials and methods summary

A detailed description of the materials and methods is available in the supplementary materials.

Mouse lines

The mouse lines used were NOD-scid γc−/− (NSG) mice (Jackson Laboratory, Bar Harbor, ME, USA, RRID: IMSR_JAX:005557) and 1-C57BL/NCrl mice (Charles River, strain code 027). All procedures involving mice were performed in accordance with the Swiss Federal Veterinary Office guidelines and the Cantonal Veterinary Office Zürich or the Cantonal Veterinary Office Basel guidelines, respectively, and were approved under the license numbers ZH159/2017 and ZH133/2021 (NSG mice) and 3112_33316 (1-C57BL/NCrl mice).

NSG mice were bred and maintained at the Institute of Experimental Immunology of the University of Zürich. The housing conditions were: ambient temperature 21° to 24°C, humidity 35 to 70%, 12-hour light-dark cycles, T 2L individually ventilated cages. The diet was Kilba Nafag maintenance extrudate for mice and rats (product no. 3436). The minimum number of males used was one, and the minimum number for females was two. The maximum number of animals per cage was five, the minimum number per cage was two animals. Cages were enriched with small houses, crinkled sterilized carton, and cage-closing grid allowed climbing. Mice were euthanized by asphyxiation with CO_2, followed by exsanguination through heart puncture.

1-C57BL/NCrl mice were bred and maintained at the Department of Biomedicine of the University of Basel. The animal facility was maintained at temperatures between 21° and 25°C and relative humidity of 55% (±10%). Up to six mice were housed in individually ventilated cages (SEALSAFE PLUS GM500) with filter top lids. Bedding material consisting of wood shavings was provided in each cage to ensure a comfortable environment. Cage enrichment was provided in the form of paper nesting material and tunnels to encourage natural behavior and reduce stress. Mice were housed under 12-hour light-dark cycles and had free access to standard laboratory chow for mice and rats (Granovit AG 3436EX) as well as water throughout the experimental period. During experiments, mice were monitored every other day for signs of distress, and body weight was measured twice per week. At end point, mice were euthanized by asphyxiation with concentrated CO_2 (80 to 90%) in an inhalation chamber.

Swiss Transplant Cohort Study and patient selection

The STCS is a prospective multicenter study that enrolls all SOT recipients in Switzerland (*58*). Clinical and laboratory data are continuously collected, and biobanking is performed at the time of transplantation (t0), at 6 (t6), and 12 (t12) months posttransplantation, then yearly thereafter. The here-outlined case-control study was approved by the Scientific Committee of the STCS, which granted permission to use patient- and graft-specific data, provided PBMCs, serum samples, and access to histopathological sections of PTLD lesions. Informed consent was obtained from all participants. The study was further approved by the ethics committees Ethikkommission Zürich and Ethikkommission Nordwest- und Zentralschweiz, ref. number 2018-01109, and complies with all relevant ethical regulations. A total of 16 patients with histologically confirmed EBV-positive PTLD diagnosed between 6- and 18-months posttransplant were identified. Of these, patients with cytomegalovirus (CMV) disease, tumors other than EBV-associated lymphoma or incomplete sampling were excluded from the study. Control patients consisted of patients with EBV-positive serostatus before transplantation, matched with cases for age, sex, transplant organ type, and creatinine levels. Ten control patients with EBV reactivation between 6 and 18 months posttransplant (defined as detectable EBV DNA in peripheral blood) and 10 patients without EBV reactivation within the first 18 months posttransplant were selected.

Isolation of B cells from buffy coat preparations

B cells were obtained from buffy coat preparations of healthy donors from the regional blood donation organization Blutspendezentrum SRK beider Basel after written consent was obtained. Bulk B cells ($CD19^+$ cells) were isolated using CD19 Microbeads and naïve B cells ($CD19^+$, $CD27^-$, IgD^+) with the REAlease CD19 MicroBead kit (both Miltenyi Biotec, Germany).

Preparation of virus stock

The cell lines B95.846 and P3HR1 were induced with phorbol 12-myristate 13-acetate (PMA, Merck) at 50 ng/ml and 3 mM butyric acid (Sigma-Aldrich) for 4 days to release virus. Virus was concentrated by speed-centrifugation titrated on B cells and by BALF5 quantitative polymerase chain reaction (qPCR) (59). For in vivo experiments, EBV B95-8-GFP (EBVwt, p2089) was produced in human embryonic kidney 293T cells, as described previously (60, 61).

Infection of B cells

B cells were infected with EBV B95-8 or EBV P3HR1, respectively, by spinoculation as previously described (62).

Imaging flow cytometry

Cells were fixed with 4% paraformaldehyde (PFA), permeabilized with 0.3% Triton-X-100, and blocked with 5% goat serum (Sigma-Aldrich). Cells were stained with anti-EBNA2 (PE2, Abcam, RRID:AB_2049594) and counterstained with 4′,6-diamidino-2-phenylindole (DAPI). Images were acquired using the Imagestream X Mark II imaging flow cytometer (AMNIS), magnification ×60. Data were compensated and analyzed using IDEAS v.6.1 software (Amnis).

Untargeted metabolomics

Naïve, freshly isolated B cells were infected with EBV B95-8, or stimulated with h.i. EBV, for 24 or 96 hours. Metabolite extraction and metabolomic analyses were performed by Metabolon, Morrisville USA.

Immunoblot analyses

Lysates were separated by 4 to 15% Mini Protean TGX Gel (Bio-Rad) and transferred to nitrocellulose using Trans-Blot Turbo Transfer system (Bio-Rad). Membranes were probed with anti-IDO (Cell Signaling, D5J4ETM, cat. no. 86630S), anti-EBNA2 (Abcam, Pe2 RRID:AB_2049594), anti-HA (Abcam, ab9110, RRID:AB_307019), anti-IDO2 (Thermo Fisher, 703150, cat. no. 703150), anti-TDO (Abcam, ab259359), anti NAMPT (61122, Cell Signaling), anti β-Tubulin (Cell Signaling, 9F3), anti-GAPDH (Cell Signaling, D4C6R), and anti-β-Actin (Cell Signaling, 8H10D10) antibodies.

LC-MS/MS measurements

Liquid chromatography–tandem mass spectrometry (LC-MS/MS) (Shimadzu, Kyoto, Japan) connected to an API 5500 Qtrap mass spectrometer (Sciex, MA, USA) was used. All analytes were detected by multiple reaction monitoring in the positive ionization mode, except QUIN. The employed mass transitions and compound specific parameters are summarized in table S3. Analyst 1.7.2 (Sciex) software was used to operate the system. Naïve B cells were infected with B95-8 EBV as described above. For ^{13}C11-TRP tracings, tryptophan-free RPMI (Pan Biotech) was supplemented with 10% dialyzed FBS (fetal bovine serum, dialyzed; GibcoTM), 1% penicillin-streptomycin, 2% GlutaMAX, 0.5% MEM nonessential amino acid solution, 0.5% sodium pyruvate (all from GIBCO, Thermo Fisher Scientific) and 25 μM ^{13}C11-TRP (Cambridge Isotope Laboratories). For ^{13}C6-KYN tracings, cells were resuspended in LCM-10 with 10% dialyzed FBS and the indicated concentration of ^{13}C6-KYN (Alsachim). Metabolites were extracted using −20°C 80:20 methanol/water. MS data were analyzed using the software Analyst (version 1.7.2, Sciex) and all tracing data were corrected for natural abundance using the software IsoCorrectoR, version 3.14 (63).

Transformation efficiency assay

Transformation efficiency was assessed as previously described (64).

CRISPR-Cas9 editing of primary human B cells

CRISPR-Cas9 KO experiments were performed as described (65) with minor changes. For one CRISPR-Cas9 KO experiment, 75 pmol triple sgRNAs (table S6) were mixed with 60 pmol Cas9 (IDT) to form RNP complexes. A PCR product spanning the CRISPR site was generated from genomic DNA using primer pair IDO1-3 fwd (table S5) and IDO1-3 rev (table S5). The purified DNA was sequenced using IDO1 seq rev primer (table S5). Sanger sequencing results were analyzed with the Inference of CRISPR Edits (ICE) tool (66).

Flow cytometry

Cells were stained with anti-Annexin V FITC (BD Biosciences, 556420) and Propodium iodide solution (BD Biosciences, 556463). For cell surface marker expression, cells were stained with LIVE/DEAD Fixable Near-IR - Dead Cell Stain (Thermo Fisher), anti-CD38 BV711 (Biolegend, 303528), anti-CD69 FITC (ImmunoTools, 21620693), anti-HLA-DR APC (Biolegend, 307609), anti-CD27 APC (BD Pharmingen, 561400). Cells were acquired using the CytoFLEX Flow Cytometer (Beckman Coulter). Data were analyzed using FlowJo v10.8.

Cell cycle analysis

B cells were assayed for DNA content by DAPI staining and flow cytometry. Single cells were identified by using height and area signals of the side scatter as indicated in fig. S10B. Sub-G0/G1 cells, which had low PI staining, were excluded from the analysis. Cells in G0+G1, S and G2 phase were identified by manual gating on DAPI histograms, as detailed in fig. S10B.

In silico modeling of EBNA2–EBF1 interaction

Structural studies were performed using AlphaFold2 (67) in its cloud-based ColabFold implementation (68) with AlphaFold-multimer (69). Relaxation for AlphaFold2-generated structures was performed with AMBER using standard parameters (70). Production molecular dynamic simulations were run using V100 GPU Google Cloud instances in Google CoLab, using the OpenMM CoLab toolkit as described in (71), with standard AMBER parameters, in 50-ns increments, ff19SB forcefield, and TIP3P water. Figures were generated using ChimeraX (72).

EBNA-2 ChIP PCR and CBF1 and EBF1 Re-ChIP

B cells were cross-linked using UV-Stratlinker 1800 then resuspended in 1 ml TRIzol reagent (Thermo Fisher), and total genomic DNA extraction was performed according to manufacturer's instructions. Extracted DNA was resuspended in TE buffer (10 mM Tris-Cl pH 8.0, 1 mM EDTA, QIAGEN) and fragmented in a Diagenode Bioruptor sonication device. Sonication was performed with eight cycles on/off time 30″/90″ to obtain DNA fragments of 300- to 400–base pair (bp) size. DNA (500 ng) was collected in 200 μl IP buffer (10 mM sodium phosphate buffer pH 7.0, 140 mM NaCl, 0.05% Triton X-100). DNA was incubated with 5 μg anti-EBNA2 antibody (Abcam, ab90543) or anti-rabbit IgG isotype control (ab171870, abcam) for 2 hours at 4°C, shaking. Protein A/G magnetic beads (Thermo Fisher) were prepared by washing twice with IP buffer. Washed beads (30 μl) were added to the DNA and incubated for overnight at 4°C, shaking. After incubation, IP reaction was washed twice with IP buffer and resuspended in 500 μl digestion buffer (50 mM Tris-HCL pH 8.0, 10 mM EDTA pH 8.0, 0.5% SDS) supplemented with 100 μg proteinase K (Thermo Fisher) and incubated for 2 hours at 56°C. IP product was then collected and purified using QIAquick PCR purification kit (QIAGEN) according to manufacturer's instructions. EBNA2-ChIP was validated by standard PCR using primers in table S5 (IDT). For Re-ChIP experiments, EBNA2-IP-DNA was incubated with 5 μg anti-CBF1 (RBPJk) (Abcam, EPR13479) and anti-EBF1 antibody (Cell Signaling, #50752) or anti-rabbit IgG isotype control (Abcam, ab171870) for 2 hours at 4°C, shaking. Fold enrichment was calculated using the following formula: 2^(–(deltaCt(IP)-deltaCt (IgG)). For EBNA2 ChIP–EBF1 Re-ChIP-Seq experiments, libraries were prepared with KAPA hyper-prep kit and purified with 0.8× vol SPR beads (all Roche). Sequencing was performed by NovaSeq using an SP flowcell yielding 30 M reads.

EBNA2-inducible system

The DG75$^{ER/EBNA2}$ CBF1-WT (C5) and CBF1-KO (C2) cells carrying the ER/EBNA2 (estrogen receptor hormone binding domain EBNA2) fusion protein (38)—a kind gift from Bettina Kempkes, LMU Munich—were used. During the 4 days of β-estradiol depletion DNA-hypomethylation was induced by addition of 2 μM 5-aza-2′-deoxycytidine (A3654, Sigma-Aldrich) to the cells each day. The ER/EBNA2 fusion protein was activated by addition of 1 μM β-estradiol overnight.

Methylated DNA immunoprecipitation (Me-DIP)

Sonication was performed with Diagenode Bioruptor sonication device eight cycles on/off time 5″/90″. Me-DIP was performed as previously described using 5 μg anti-5-methylcytosine (5-mC) rabbit monoclonal antibody or anti-rabbit IgG isotype control (ab171870, Abcam) (73). Validation of Me-DIP was done by PCR using the primers indicated in table S5 (all from IDT). Me-DIP was validated by qPCR using the GoTaq SYBR Green kit (Promega) according to manufacturer's instructions. Fold enrichment was calculated using the formula 2^(-(deltaCt(IP)-deltaCt(IgG)).

RNA-seq

RNA was isolated using the nucleospin RNA kit (Macherey-Nagel). RNA-seq was performed by Admera Health. Reads were aligned to the human genome (UCSC version hg38 analysis set; http://genome.ucsc.edu) with STAR (74) (version 2.5.2a or version 2.7.10a) with default parameters except for allowing up 10 hits to genome (outFilterMultimapNmax 10), reporting only one location for hits with equal score (outSAMmultNmax 1), and for filtering reads without evidence in spliced junction table (outFilterType "BySJout"). The output was sorted and indexed with samtools (75) (v 1.7). Strand-specific coverage tracks per sample were generated by tiling the genome in 20-bp windows and counting 5′ end of reads per window using the function bamCount from the Bioconductor package bamsignals (v1.10.0). These window counts were exported in bigWig format using the Bioconductor package rtracklayer (76) (v1.38.3). Read and alignment quality was evaluated using the qQCReport function of the Bioconductor package QuasR (77) (v 1.18.0). The featureCounts function from Bioconductor package Rsubread (v 1.28.1) was used to count the number of read (5′ ends) overlapping with the exons of each gene assuming an exon union model (with used gene model provided by UCSC RefSeq Track from 2017-09-01). For the dataset from IDO1-inhibited B cells, the subread (version 2.0.1) was used to count the number of reads (5′ ends) overlapping with the exons of each gene assuming an exon union model (with used gene model provided by ensemble version 104). Data were normalized by applying the TMM method from Bioconductor edgeR (78) package (versions 3.20.9 and 3.36.0, respectively). Only genes having $\log_2$ CPM counts bigger than 0 in at least two samples were kept for further analyses. The principal components analysis was based on 25% of most variable genes in the dataset. Differentially expressed genes were identified using the quasi-likelihood (QL) method implemented in edgeR package using patient id as a covariate. Genes with a false discovery rate (FDR) of ≤0.05 and minimum log fold change of 2 were considered as differentially expressed.

For transcriptome analysis involving IDO1 blockade, bulk B cells were isolated as described above and either infected with EBV, stimulated with h.i. EBV, or stimulated with 2.5 μg/ml CpG (ODN 2006, ODN 7990, no. 6057-42-01 from InvivoGen), or activated by BCR cross-linking using goat-anti-human IgA, IgG, and IgM (H+L) at a concentration of 5 μg/ml (no. 109-006-064 from Jackson Immunoresearch) for 2 days. Lin. was added at the day of infection or stimulation at a concentration of 10 μM. RNA-seq was performed at the Department of Biosystems Science and Engineering, ETH Zurich, in paired-end mode on an Illumina NextSeq 500 with 38 cycles. The raw reads were aligned against the NCBI human GRCh38 assembly using STAR version 2.7.9a in paired-end mode. The read counts of each sample were summarized using featureCounts from the Subread package using strand information and the NCBI GRCh38 annotations. Differential gene expression was analyzed using DESeq2 version 1.38.2. Gene biotype and gene symbol annotation was fetched from Ensemble using biomaRt version 2.54.1. Protein coding genes and genes with >10 reads in at least three samples were kept. Transcription changes due to batch effects were corrected for using the removeBatchEffect function of limma version 3.54.2. Volcano plot was drawn with a significance cutoff at 0.05 adjusted *P* value. Calculations were performed with sciCORE scientific computing center at University of Basel.

Extracellular flux analyses

For analysis of oxygen consumption rate (OCR; pmol/min) and extracellular acidification rate (ECAR; mpH/min) a Seahorse XF-96 extracellular flux analyzer was used (Seahorse Bioscience, Agilent Technologies) as previously described (79).

HA-IDO1 overexpression in LCLs

pcDNA3.1 plasmids encoding IDO1 with an N- or C-terminal HA-tag under a CMV promoter were synthesized by Gene Script and transfected into LCLs followed by selection with G-418 solution (Sigma-Aldrich). Cells were probed for HA and IDO1 expression by immunoblotting.

His-EBNA2 overexpression in Ramos cells

A codon optimized EBNA2 cDNA with a C-terminal His-tag was cloned into the Lentivector pLeGO-hEμMAR-iG2 (Addgene #52635, a kind gift from J. Mautner). For stable EBNA2 expression, Ramos cells were transduced with lentiviral particles by spinoculation. Lentivirally transduced cells were sorted for IRES-driven eGFP expression before expansion.

Respiratory chain complex activiy biochemical assays

Activity of individual mitochondrial respiratory chain complexes was performed in Lin.-treated and vehicle-treated EBV-infected B cells at 2 days pi using enzyme-linked immunosorbent assay microplate assay kits (Abcam) according to the manufacturer's instructions.

ADP/ATP ratio determination

ADP/ATP ratio was determined using an Assay Kit (Sigma-Aldrich).

Electron microscopy

Cells were fixed in 4% PFA, 5% glutaraldehyde, in 0.1M PIPES buffer pH 7.0 to 7.2 for 15 min followed by 2% PFA, 2.5% glutaraldehyde, in 0.1M PIPES buffer pH 7.0 to 7.2 for another 45 min, embedded, and then cut into 60-nm sections. Micrographs (27,000× magnification) were obtained with a Tecnai G2 Spirit (FEI) transmission electron microscope equipped with an EMSIS Veleta camera (top, side-mounted) operated at 80 kV using RADIUS software from EMSIS. ImageJ software (NIH) was used to assess the number of mitochondria per cell and percentage of aberrant mitochondria as well as mitochondrial length (major axis) and width (minor axis). The aspect ratio of mitochondria was calculated as "major axis" over "minor axis," with an aspect ratio of 1 indicating a circular mitochondrial section.

Cytometry by time of flight

Cell barcoding and labeling was performed as per manufacturer recommendations (Standard Biotools). Surface antibody cocktail consisting of 21 metal-conjugated antibodies and 500 μM 103Rhodium Live/Dead was used (Standard Biotools or self-conjugated using Maxpar X8 Antibody Labeling kits (Standard Biotools) (table S4). For acquisition, a Helios CyTOF system (Standard Biotools, CA) was used. Data were collected as .fcs files using CyTOF software (Version 6.7.1014, Standard Biotools). After acquisition, files were concatenated and normalized to the acquired calibration bead signal and individual files were stored into .fcs files using CyTOF software. Data cleanup was performed by Gaussian distribution exclusion method and de-barcoding was performed by Boolean-gating using FlowJo (Version 9.0.1).

Humanized mouse model of EBV infection

Newborn NSG pups, up to 5 days of age, were sublethally irradiated with 1 Gy and injected intrahepatically with 1×10^5 to 3×10^5 $CD34^+$ hematopoietic progenitor and stem cells (HPSC) purified from human fetal liver (HFL) tissue, obtained from Advanced Bioscience Resources. Three months later, the level of human immune system engraftment was assessed by flow cytometry (CD45, CD3, CD4, CD8, CD19, and NKp46) (fig. S3A). Three- to five-month old female and male animals were intraperitoneally infected with 10^5 B95-8 or P3HR1 EBV Raji Green Units (RGU) or PBS control. Beginning 3 or 7 days before infection, mice were treated with Epa. or KHK2455 for 2 or 5 weeks pi, as indicated, or with vehicle. Epa. was administered either by daily intraperitoneal injections (200 mg/kg) or in drinking water (100 mg/kg), as indicated. KHK2455 was administered at 10 mg/kg in drinking water. Tumor incidence was determined by macroscopical inspection of the peritoneum and organs during euthanasia and confirmed by EBER in situ hybridization. EBV loads were assessed in DNA preparations from whole blood at week 2, 3, 4, and 5 pi and in the spleen on the day of euthanasia, using Taqman real-time PCR with modified primers and a fluorogenic probe, as detailed in table S5, to detect the conserved EBV BamHI-W fragment. Samples were analyzed in triplicates and run on a CFX384 Touch Real-time PCR Detection System (Bio-Rad). DNA from whole blood was extracted with the NucliSENS EasyMAG System (Biomérieux), and DNA from splenic tissues was isolated using the DNeasy Blood and Tissue kit (QIAGEN), according to the manufacturer's recommendations. Human immune cell composition was monitored in the blood one week before infection, as well as at weeks 2, 3, 4, and 5 pi and in splenocytes on the day of euthanasia. For immunophenotyping, cell suspensions were stained for 20 min at 4°C with: CD45 (clone HI30), CD8 (clone RPA-T8), CD4 (clone SK3), NKp46 (clone 9E2/NKp46), all from BD; HLA-DR (clone L243), CD45RA (clone HI100), CD3 (clone OKT3), CD62L (clone DREG-56), CD27 (clone O323), CD19 (clone HIB19), CD39 (clone A1), CD70 (clone 113-16), Zombie Aqua Fixable Viability kit, all from Biolegend; IgD (clone IADB6) from Southern Biotech; and CD19 (clone SJ25-C1) and CD23 (clone EBVCS2) from Thermo Fisher, then fixed with 1% PFA for 30 min, before acquisition on a BD FACSymphony (BD Biosciences). Data analysis was performed using FlowJo software (FlowJo LLC).

Adoptive transfer of in vitro infected B cells into NOD-scid $\gamma c^{-/-}$ (NSG) mice

Three- to five-month-old nonreconstituted NSG mice were used for the adoptive transfer of in vitro–infected bulk B cells isolated from buffy coat preparations. IDO1-KO or scrambled guide RNA–treated B cells were generated as described above, and infected with B95-8 EBV at an MOI of 0.5. WT B cells were infected with P3HR1 EBV or B95-8 EBV at an MOI of 1, as indicated. After addition of the virus, cells were centrifuged for 30 min at 800g, 4°C, then incubated for 1.5 hours at 37°C before being collected, washed, and resuspended in PBS for injection. Infected B cells (4×10^6) were injected intraperitoneally in 200 μl of PBS. Mice receiving IDO1-KO and scrambled control B cells were sacrificed after 4 weeks. Mice receiving P3HR1-infected B cells were euthanized after 7 days of infection. Tumors were enumerated macroscopically and confirmed by EBER in situ hybridization. Isolation of genomic DNA from tumors was done using Quick-DNA/RNA MiniPrep Plus Kit (Zymo Research). A PCR product was generated, spanning the CRISPR site with IDO1-3 fwd and IDO1-3 rev (table S5). The purified DNA was sequenced using IDO1 seq rev primer (table S5). Sanger sequencing results were analyzed with ICE tool (66).

T cell activation in C57BL/6 mice with anti-CD3ε F(ab')2 fragment

Ten- to twelve-week-old 1-C57BL/NCrl mice were administered Epa. at 100 mg per kg per day or vehicle control in drinking water for 7 days. On day 7, each mouse received 5 μg anti-CD3ε F(ab')2 fragment (BioXCell) by tail-vein injection. Six hours after injection, blood was collected by heart puncture into EDTA tubes (Sarsted) and spleens were harvested. Blood and spleen cells were analyzed by flow cytometry using the following markers: CD3 (17A2), CD4 (GK1.5), CD8 (53-6.7), CD27 (LG.3A10), CD28 (37.51) CD62L (MEK-14), CD69 (H1.2F3) (all BioLegend); CD45RA (14.8, BD Bioscience); and Live/Dead Zombie UV Fixable Viability Kit (BioLegend), using a BD Fortessa LSR II (BD Bioscience) flow cytometer.

Immunohistochemistry of patient and mouse tumor sections

Biopsies were fixed in 10% neutral buffered formalin, embedded in paraffin and stained with hematoxylin and eosin (H&E). Immunohistochemistry and in situ hybridization were performed on serial tissue sections using an automated immunostainer Benchmark XT (Ventana/Roche, Tucson, AZ, USA) according to routine procedures. EBV was detected by in situ hybridization with EBERs (Ventana 800-2842, prediluted). Expression of IDO1, EBNA2, and LMP1 was probed with the following monoclonal antibodies: IDO1 (D5J4E, Cell Signaling), EBNA2 (Abcam, clone PE2), and LMP1 (Ventana 760-2640). Brightfield images of tumor sections were taken with a 10× objective (CFI Plan Apo Lambda, NA 0.45) on a Nikon Ti2, equipped with a Nikon DS-Ri2 CMOS camera. Images were processed with FIJI software.

LC-MS measurements of patients' sera

Metabolite extraction was performed from 20 μl of serum with 100 μl of 4:1 methanol: water containing 2 μM [$^{13}C_{10}$, $^{15}N_5$] adenosine monophosphate, 10 μM [$^{13}C_4$] succinic acid, 50 nM $^{13}C_5$ inosine, and a 1 in 5000 diluted [$U^{13}C_{10}$, $U^{15}N_5$] mixture of amino acid was added (all available from Sigma). A Q Exactive Plus orbitrap coupled to a Vanquish Horizon ultra-high-performance liquid chromatography system was used for all the analysis (both from Thermo Fisher Scientific). Analysis was carried out using an ACE Excel C18-PFP column (150 × 2.1 mm, 2.0 μm, Hichrom). Source parameters used for the mass spectrometer were a vaporizer temperature of 450°C and ion transfer tube temperature of 320°C, an ion spray voltage of 3.5 kV (2.5 kV for negative ion mode) and a sheath gas of 55, auxiliary gas of 15 and a sweep gas of 3 arbitrary units with an S-lens RF (radio frequency) of 50%. For MS analysis, a full scan of 60-900 *m/z* was used for positive ion mode at a resolution of 70,000 ppm. The negative ion mode scan was >80 to 900 *m/z* at the same resolution. All data were acquired using Xcalibur (Version 4.1, Thermo Fisher Scientific). Unbiased analysis was carried out using Compound Discoverer (Version 3.1, Thermo Fisher Scientific). For unbiased analysis, metabolites were verified using the high-resolution *m/z* METLIN database (Scripps Research Institute). Peak areas corresponding to metabolite levels were normalized to total ion content and presented as relative areas. Accurate *m/z* values were compared against the METLIN database (Scripps Research Institute), including $[M+H]^+$, $[M+Na]^+$, and $[M+NH_4]^+$ for positive mode and $[M-H]^-$ and $[M+Cl]^-$ for negative mode ion adducts with a mass tolerance of 2 ppm. Targeted analysis was carried out using Xcalibur, with compounds of interest normalized to an appropriate internal standard and the area ratio thus obtained compared with that in the relevant calibration line. All data were collated using Excel (2016 version, Microsoft).

EBV CTL expansion and flow cytometric analysis

EBV-transformed LCLs were generated as previously described (*80*). On days 17 and 35, cells were harvested for intracellular cytokine staining, anti-CD107a-BV605 (H4A3, BioLegend), and co-stimulatory anti-CD28/CD49d Mabs (1 μg/ml) (BD Fastimmune). Cells were stimulated with PepTivator EBV Consensus peptide mix (0.1 μg per peptide per ml) (Miltenyi Biotech). After 1 hour of incubation (37°C, 5% CO_2), brefeldin A (10 mg/ml) (Sigma Aldrich) was added to each well, and cells were incubated for another 5 hours. Afterwards, cells were stained for viability by Zombie UV fixable dye (BioLegend), washed twice, then stained for CD3 (UCHT1), CD4 (SK3), and CD8 (SK1) (all from BD Biosciences); and CD69 (FN50), IFNγ (B27), TNF (Mab11), Granzyme B (QA16A02) (all from BioLegend). Data were acquired by spectral flow cytometry (Cytek Aurora, Cytek Biosciences) and analyzed by FlowJo software (FlowJo LLC) version 10.8.0.

Statistical analyses

Statistical analyses were performed with Prism software version 9.2.0 and R software version 3.6.3. Data are shown as individual data points where applicable, normally distributed data are shown as mean ± SD, non-normally distributed data as median ± interquartile range (IQR) or 95% CI. Box and whisker plots indicate mean or median, and max. and min. values. Violin plots indicate median, IQR, and range; medium smoothing by kernel density estimator was applied. Data were subjected to repeated Grubbs' test to identify the presence of outlier data points. For paired and unpaired data comparison two-tailed Student's t test was used. Three or more groups were compared using a repeated measures or a one-way analysis of variance (ANOVA) test followed by multiple comparisons test to compare individual groups. Frequencies in more than one category were analyzed by contingency tables and chi-square test. Receiver operating characteristic (ROC) curve analyses were performed in R (Version 4.1.0) by creating a generalized linear model with a nominal logistic regression. The ROC analysis was then calculated using the pROC package and logcodens smoothing was applied to the resulting curves. P values of <0.05 were considered statistically significant.

REFERENCES AND NOTES

1. S. Tzellos, P. J. Farrell, Epstein-Barr virus sequence variation—biology and disease. *Pathogens* **1**, 156–174 (2012). doi: 10.3390/pathogens1020156; pmid: 25436768
2. S. Halder *et al*., Early events associated with infection of Epstein-Barr virus infection of primary B-cells. *PLOS ONE* **4**, e7214 (2009). doi: 10.1371/journal.pone.0007214; pmid: 19784370
3. J. I. Cohen, F. Wang, J. Mannick, E. Kieff, Epstein-Barr virus nuclear protein 2 is a key determinant of lymphocyte transformation. *Proc. Natl. Acad. Sci. U.S.A.* **86**, 9558–9562 (1989). doi: 10.1073/pnas.86.23.9558; pmid: 2556717
4. G. J. Babcock, L. L. Decker, M. Volk, D. A. Thorley-Lawson, EBV persistence in memory B cells in vivo. *Immunity* **9**, 395–404 (1998). doi: 10.1016/S1074-7613(00)80622-6; pmid: 9768759
5. G. S. Taylor, H. M. Long, J. M. Brooks, A. B. Rickinson, A. D. Hislop, The immunology of Epstein-Barr virus–induced disease. *Annu. Rev. Immunol.* **33**, 787–821 (2015). doi: 10.1146/annurev-immunol-032414-112326; pmid: 25706097
6. C. Shannon-Lowe, A. B. Rickinson, A. I. Bell, Epstein-Barr virus-associated lymphomas. *Philos. Trans. R. Soc. London Ser. B* **372**, 20160271 (2017). doi: 10.1098/rstb.2016.0271; pmid: 28893938
7. P. J. Farrell, Epstein-Barr virus and cancer. *Annu. Rev. Pathol.* **14**, 29–53 (2019). doi: 10.1146/annurev-pathmechdis-012418-013023; pmid: 30125149
8. G. Miller, J. Robinson, L. Heston, Immortalizing and nonimmortalizing laboratory strains of Epstein-Barr virus. *Cold Spring Harb. Symp. Quant. Biol.* **39**, 773–781 (1975). doi: 10.1101/SQB.1974.039.01.089; pmid: 169031
9. G. Miller, J. Robinson, L. Heston, M. Lipman, Differences between laboratory strains of Epstein-Barr virus based on immortalization, abortive infection, and interference. *Proc. Natl. Acad. Sci. U.S.A.* **71**, 4006–4010 (1974). doi: 10.1073/pnas.71.10.4006; pmid: 4372601
10. C. Li *et al*., EBNA2-deleted Epstein-Barr virus (EBV) isolate, P3HR1, causes Hodgkin-like lymphomas and diffuse large B cell lymphomas with type II and Wp-restricted latency types in humanized mice. *PLOS Pathog.* **16**, e1008590 (2020). doi: 10.1371/journal.ppat.1008590; pmid: 32542010
11. D. Dierickx, T. M. Habermann, Post-transplantation lymphoproliferative disorders in adults. *N. Engl. J. Med.* **378**, 549–562 (2018). doi: 10.1056/NEJMra1702693; pmid: 29414277
12. Q. Y. Zhu *et al*., A potent and protective human neutralizing antibody targeting a novel vulnerable site of Epstein-Barr virus. *Nat. Commun.* **12**, 6624 (2021). doi: 10.1038/s41467-021-26912-6; pmid: 34785638
13. X. Zhang *et al*., Protective anti-gB neutralizing antibodies targeting two vulnerable sites for EBV-cell membrane fusion. *Proc. Natl. Acad. Sci. U.S.A.* **119**, e2202371119 (2022). doi: 10.1073/pnas.2202371119; pmid: 35917353
14. J. Snijder *et al*., An antibody targeting the fusion machinery neutralizes dual-tropic infection and defines a site of vulnerability on Epstein-Barr virus. *Immunity* **48**, 799–811.e9 (2018). doi: 10.1016/j.immuni.2018.03.026; pmid: 29669253
15. E. González-Barca *et al*., Prospective phase II trial of extended treatment with rituximab in patients with B-cell post-transplant lymphoproliferative disease. *Haematologica* **92**, 1489–1494 (2007). doi: 10.3324/haematol.11360; pmid: 18024397
16. S. Choquet *et al*., Rituximab in the management of post-transplantation lymphoproliferative disorder after solid organ transplantation: Proceed with caution. *Ann. Hematol.* **86**, 599–607 (2007). doi: 10.1007/s00277-007-0298-2; pmid: 17522862
17. R. Trappe *et al*., Sequential treatment with rituximab followed by CHOP chemotherapy in adult B-cell post-transplant lymphoproliferative disorder (PTLD): The prospective international multicentre phase 2 PTLD-1 trial. *Lancet Oncol.* **13**, 196–206 (2012). doi: 10.1016/S1470-2045(11)70300-X; pmid: 22173060
18. L. W. Wang *et al*., Epstein-Barr-virus-induced one-carbon metabolism drives B cell transformation. *Cell Metab.* **30**, 539–555.e11 (2019). doi: 10.1016/j.cmet.2019.06.003; pmid: 31257153
19. L. W. Wang *et al*., Epstein-Barr virus subverts mevalonate and fatty acid pathways to promote infected B-cell proliferation and survival. *PLOS Pathog.* **15**, e1008030 (2019). doi: 10.1371/journal.ppat.1008030; pmid: 31518366
20. A. Y. Hafez *et al*., Limited nucleotide pools restrict Epstein–Barr virus-mediated B-cell immortalization. *Oncogenesis* **6**, e349 (2017). doi: 10.1038/oncsis.2017.46; pmid: 28604764
21. K. McFadden *et al*., Metabolic stress is a barrier to Epstein-Barr virus-mediated B-cell immortalization. *Proc. Natl. Acad. Sci. U.S.A.* **113**, E782–E790 (2016). doi: 10.1073/pnas.1517141113; pmid: 26802124
22. K. Ladell *et al*., Immune activation suppresses initiation of lytic Epstein-Barr virus infection. *Cell. Microbiol.* **9**, 2055–2069 (2007). doi: 10.1111/j.1462-5822.2007.00937.x; pmid: 17419714
23. P. Mrozek-Gorska *et al*., Epstein-Barr virus reprograms human B lymphocytes immediately in the prelatent phase of infection. *Proc. Natl. Acad. Sci. U.S.A.* **116**, 16046–16055 (2019). doi: 10.1073/pnas.1901314116; pmid: 31341086
24. A. J. Sinclair, I. Palmero, G. Peters, P. J. Farrell, EBNA-2 and EBNA-LP cooperate to cause G0 to G1 transition during immortalization of resting human B lymphocytes by Epstein-Barr virus. *EMBO J.* **13**, 3321–3328 (1994). doi: 10.1002/j.1460-2075.1994.tb06634.x; pmid: 8045261
25. P. S. Minhas *et al*., Macrophage de novo NAD^+ synthesis specifies immune function in aging and inflammation. *Nat. Immunol.* **20**, 50–63 (2019). doi: 10.1038/s41590-018-0255-3; pmid: 30478397
26. N. Braidy, G. J. Guillemin, H. Mansour, T. Chan-Ling, R. Grant, Changes in kynurenine pathway metabolism in the brain, liver and kidney of aged female Wistar rats. *FEBS J.* **278**, 4425–4434 (2011). doi: 10.1111/j.1742-4658.2011.08366.x; pmid: 22032336
27. A. A. Badawy, G. Guillemin, The plasma [kynurenine]/[tryptophan] ratio and indoleamine 2,3-dioxygenase: Time for appraisal. *Int. J. Tryptophan Res.* **12**, 1–10 (2019). doi: 10.1177/1178646919868978; pmid: 31488951
28. A. Balog *et al*., preclinical characterization of linrodostat mesylate, a novel, potent, and selective oral indoleamine 2,3-dioxygenase 1 inhibitor. *Mol. Cancer Ther.* **20**, 467–476 (2021). doi: 10.1158/1535-7163.MCT-20-0251; pmid: 33298590
29. E. W. Yue *et al*., INCB24360 (epacadostat), a highly potent and selective indoleamine-2,3-dioxygenase 1 (IDO1) inhibitor for immuno-oncology. *ACS Med. Chem. Lett.* **8**, 486–491 (2017). doi: 10.1021/acsmedchemlett.6b00391; pmid: 28523098
30. T. A. Yap *et al*., First-in-human study of KHK2455, a long-acting, potent and selective indoleamine 2,3-dioxygenase 1 (IDO-1) inhibitor, in combination with mogamulizumab (Moga), an anti-CCR4 monoclonal antibody, in patients (pts) with advanced solid tumors. *J. Clin. Oncol.* **36** (suppl.), 3040 (2018). doi: 10.1200/JCO.2018.36.15_suppl.3040
31. G. V. Long *et al*., Epacadostat plus pembrolizumab versus placebo plus pembrolizumab in patients with unresectable or metastatic melanoma (ECHO-301/KEYNOTE-252): A phase 3, randomised, double-blind study. *Lancet Oncol.* **20**, 1083–1097 (2019). doi: 10.1016/S1470-2045(19)30274-8; pmid: 31221619
32. G. Sonpavde *et al*., ENERGIZE: A Phase III study of neoadjuvant chemotherapy alone or with nivolumab with/without linrodostat mesylate for muscle-invasive bladder cancer. *Future Oncol.* **16**, 4359–4368 (2020). doi: 10.2217/fon-2019-0611; pmid: 31823654
33. P. A. Nikitin, A. M. Price, K. McFadden, C. M. Yan, M. A. Luftig, Mitogen-induced B-cell proliferation activates Chk2-dependent G1/S cell cycle arrest. *PLOS ONE* **9**, e87299 (2014). doi: 10.1371/journal.pone.0087299; pmid: 24498068
34. M. A. Rabbani, M. Ribaudo, J. T. Guo, S. Barik, Identification of interferon-stimulated gene proteins that inhibit human parainfluenza virus type 3. *J. Virol.* **90**, 11145–11156 (2016). doi: 10.1128/JVI.01551-16; pmid: 27707917
35. R. Mao *et al*., Indoleamine 2,3-dioxygenase mediates the antiviral effect of gamma interferon against hepatitis B virus in human hepatocyte-derived cells. *J. Virol.* **85**, 1048–1057 (2011). doi: 10.1128/JVI.01998-10; pmid: 21084489
36. F. Li, H. Karlsson, Antiviral effect of IDO in mouse fibroblast cells during influenza virus infection. *Viral Immunol.* **30**, 542–544 (2017). doi: 10.1089/vim.2016.0140; pmid: 28402179
37. T. Henkel, P. D. Ling, S. D. Hayward, M. G. Peterson, Mediation of Epstein-Barr virus EBNA2 transactivation by recombination signal–binding protein J_κ. *Science* **265**, 92–95 (1994). doi: 10.1126/science.8016657; pmid: 8016657
38. L. V. Glaser *et al*., EBF1 binds to EBNA2 and promotes the assembly of EBNA2 chromatin complexes in B cells. *PLOS Pathog.* **13**, e1006664 (2017). doi: 10.1371/journal.ppat.1006664; pmid: 28968461
39. S. R. Grossman, E. Johannsen, X. Tong, R. Yalamanchili, E. Kieff, The Epstein–Barr virus nuclear antigen 2 transactivator is directed to response elements by the J_κ recombination signal binding protein. *Proc. Natl. Acad. Sci. U.S.A.* **91**, 7568–7572 (1994). doi: 10.1073/pnas.91.16.7568; pmid: 8052621
40. U. Klein, K. Rajewsky, R. Küppers, Human immunoglobulin (Ig) M^+IgD^+ peripheral blood B cells expressing the CD27 cell

surface antigen carry somatically mutated variable region genes: CD27 as a general marker for somatically mutated (memory) B cells. *J. Exp. Med.* **188**, 1679–1689 (1998). doi: 10.1084/jem.188.9.1679; pmid: 9802980

41. C. T. Styles *et al*., EBV epigenetically suppresses the B cell-to-plasma cell differentiation pathway while establishing long-term latency. *PLOS Biol.* **15**, e2001992 (2017). doi: 10.1371/journal.pbio.2001992; pmid: 28771465
42. Swiss Transplant Cohort Study; https://www.stcs.ch/about/study-description.
43. A. Murer *et al*., MicroRNAs of Epstein-Barr virus attenuate T-cell-mediated immune control *in vivo*. *mBio* **10**, e01941-18 (2019). doi: 10.1128/mBio.01941-18; pmid: 30647153
44. N. Caduff *et al*., Immunosuppressive FK506 treatment leads to more frequent EBV-associated lymphoproliferative disease in humanized mice. *PLOS Pathog.* **16**, e1008477 (2020). doi: 10.1371/journal.ppat.1008477; pmid: 32251475
45. H. Zdimerova *et al*., Attenuated immune control of Epstein–Barr virus in humanized mice is associated with the multiple sclerosis risk factor HLA-DR15. *Eur. J. Immunol.* **51**, 64–75 (2021). doi: 10.1002/eji.202048655; pmid: 32949466
46. M. F. Callan *et al*., Large clonal expansions of CD8$^+$ T cells in acute infectious mononucleosis. *Nat. Med.* **2**, 906–911 (1996). doi: 10.1038/nm0896-906; pmid: 8705861
47. B. Chatterjee *et al*., CD8+ T cells retain protective functions despite sustained inhibitory receptor expression during Epstein-Barr virus infection in vivo. *PLOS Pathog.* **15**, e1007748 (2019). doi: 10.1371/journal.ppat.1007748; pmid: 31145756
48. T. Strowig *et al*., Priming of protective T cell responses against virus-induced tumors in mice with human immune system components. *J. Exp. Med.* **206**, 1423–1434 (2009). doi: 10.1084/jem.20081720; pmid: 19487422
49. Y. Deng *et al*., CD27 is required for protective lytic EBV antigen–specific CD8$^+$ T-cell expansion. *Blood* **137**, 3225–3236 (2021). doi: 10.1182/blood.2020009482; pmid: 33827115
50. D. H. Munn *et al*., Prevention of allogeneic fetal rejection by tryptophan catabolism. *Science* **281**, 1191–1193 (1998). doi: 10.1126/science.281.5380.1191; pmid: 9712583
51. D. H. Munn *et al*., GCN2 kinase in T cells mediates proliferative arrest and anergy induction in response to indoleamine 2,3-dioxygenase. *Immunity* **22**, 633–642 (2005). doi: 10.1016/j.immuni.2005.03.013; pmid: 15894280
52. S. Rad Pour *et al*., Exhaustion of CD4+ T-cells mediated by the kynurenine pathway in melanoma. *Sci. Rep.* **9**, 12150 (2019). doi: 10.1038/s41598-019-48635-x; pmid: 31434983
53. A. C. Newman *et al*., Immune-regulated IDO1-dependent tryptophan metabolism is source of one-carbon units for pancreatic cancer and stellate cells. *Mol. Cell* **81**, 2290–2302.e7 (2021). doi: 10.1016/j.molcel.2021.03.019; pmid: 33831358
54. C. A. Opitz *et al*., The therapeutic potential of targeting tryptophan catabolism in cancer. *Br. J. Cancer* **122**, 30–44 (2020). doi: 10.1038/s41416-019-0664-6; pmid: 31819194
55. K. Tang, Y. H. Wu, Y. Song, B. Yu, Indoleamine 2,3-dioxygenase 1 (IDO1) inhibitors in clinical trials for cancer immunotherapy. *J. Hematol. Oncol.* **14**, 68 (2021). doi: 10.1186/s13045-021-01080-8; pmid: 33883013
56. M. L. Nijland, M. J. Kersten, S. T. Pals, F. J. Bemelman, I. J. Ten Berge, Epstein-Barr virus–positive posttransplant lymphoproliferative disease after solid organ transplantation: Pathogenesis, clinical manifestations, diagnosis, and management. *Transplant. Direct* **2**, e48 (2015). doi: 10.1097/TXD.0000000000000557; pmid: 27500242
57. S. I. Tracy *et al*., Persistence of Epstein-Barr virus in self-reactive memory B cells. *J. Virol.* **86**, 12330–12340 (2012). doi: 10.1128/JVI.01699-12; pmid: 22951828
58. M. T. Koller *et al*., Design and methodology of the Swiss Transplant Cohort Study (STCS): A comprehensive prospective nationwide long-term follow-up cohort. *Eur. J. Epidemiol.* **28**, 347–355 (2013). doi: 10.1007/s10654-012-9754-y; pmid: 23546766
59. H. Kimura *et al*., Quantitative analysis of Epstein-Barr virus load by using a real-time PCR assay. *J. Clin. Microbiol.* **37**, 132–136 (1999). doi: 10.1128/JCM.37.1.132-136.1999; pmid: 9854077
60. H. J. Delecluse, T. Hilsendegen, D. Pich, R. Zeidler, W. Hammerschmidt, Propagation and recovery of intact, infectious Epstein-Barr virus from prokaryotic to human cells. *Proc. Natl. Acad. Sci. U.S.A.* **95**, 8245–8250 (1998). doi: 10.1073/pnas.95.14.8245; pmid: 9653172
61. R. Feederle *et al*., The Epstein-Barr virus lytic program is controlled by the co-operative functions of two transactivators. *EMBO J.* **19**, 3080–3089 (2000). doi: 10.1093/emboj/19.12.3080; pmid: 10856251
62. M. Dorner *et al*., Distinct ex vivo susceptibility of B-cell subsets to Epstein-Barr virus infection according to differentiation status and tissue origin. *J. Virol.* **82**, 4400–4412 (2008). doi: 10.1128/JVI.02630-07; pmid: 18321980
63. P. Heinrich *et al*., Correcting for natural isotope abundance and tracer impurity in MS-, MS/MS- and high-resolution-multiple-tracer-data from stable isotope labeling experiments with IsoCorrectoR. *Sci. Rep.* **8**, 17910 (2018). doi: 10.1038/s41598-018-36293-4; pmid: 30559398
64. E. Henderson, G. Miller, J. Robinson, L. Heston, Efficiency of transformation of lymphocytes by Epstein-Barr virus. *Virology* **76**, 152–163 (1977). doi: 10.1016/0042-6822(77)90292-6; pmid: 189490
65. K. Laoharawee *et al*., Genome engineering of primary human B cells using CRISPR/Cas9. *J. Vis. Exp.* **2020**, e61855 (2020). doi: 10.3791/61855; pmid: 33226023
66. D. Conant *et al*., Inference of CRISPR edits from Sanger trace data. *CRISPR J.* **5**, 123–130 (2022). doi: 10.1089/crispr.2021.0113; pmid: 35119294
67. J. Jumper *et al*., Highly accurate protein structure prediction with AlphaFold. *Nature* **596**, 583–589 (2021). doi: 10.1038/s41586-021-03819-2; pmid: 34265844
68. M. Mirdita *et al*., ColabFold: Making protein folding accessible to all. *Nat. Methods* **19**, 679–682 (2022). doi: 10.1038/s41592-022-01488-1; pmid: 35637307
69. R. Evans *et al*., Protein complex prediction with AlphaFold-Multimer. bioRxiv 2021.10.04.463034 [Preprint] (2021); https://doi.org/10.1101/2021.10.04.463034.
70. D. A. Case *et al*., The Amber biomolecular simulation programs. *J. Comput. Chem.* **26**, 1668–1688 (2005). doi: 10.1002/jcc.20290; pmid: 16200636
71. P. R. Arantes, M. D. Polêto, C. Pedebos, R. Ligabue-Braun, Making it rain: Cloud-based molecular simulations for everyone. *J. Chem. Inf. Model.* **61**, 4852–4856 (2021). doi: 10.1021/acs.jcim.1c00998; pmid: 34595915
72. E. F. Pettersen *et al*., UCSF ChimeraX: Structure visualization for researchers, educators, and developers. *Protein Sci.* **30**, 70–82 (2021). doi: 10.1002/pro.3943; pmid: 32881101
73. K. L. Thu *et al*., Methylated DNA immunoprecipitation. *J. Vis. Exp.* **2009**, e935 (2009). doi: 10.3791/935-v; pmid: 19241501
74. A. Dobin *et al*., STAR: Ultrafast universal RNA-seq aligner. *Bioinformatics* **29**, 15–21 (2013). doi: 10.1093/bioinformatics/bts635; pmid: 23104886
75. H. Li *et al*., The Sequence Alignment/Map format and SAMtools. *Bioinformatics* **25**, 2078–2079 (2009). doi: 10.1093/bioinformatics/btp352; pmid: 19505943
76. M. Lawrence, R. Gentleman, V. Carey, rtracklayer: An R package for interfacing with genome browsers. *Bioinformatics* **25**, 1841–1842 (2009). doi: 10.1093/bioinformatics/btp328; pmid: 19468054
77. D. Gaidatzis, A. Lerch, F. Hahne, M. B. Stadler, QuasR: Quantification and annotation of short reads in R. *Bioinformatics* **31**, 1130–1132 (2015). doi: 10.1093/bioinformatics/btu781; pmid: 25417205
78. M. D. Robinson, D. J. McCarthy, G. K. Smyth, edgeR: A Bioconductor package for differential expression analysis of digital gene expression data. *Bioinformatics* **26**, 139–140 (2010). doi: 10.1093/bioinformatics/btp616; pmid: 19910308
79. P. M. Gubser *et al*., Rapid effector function of memory CD8$^+$ T cells requires an immediate-early glycolytic switch. *Nat. Immunol.* **14**, 1064–1072 (2013). doi: 10.1038/ni.2687; pmid: 23955661
80. A. Merlo *et al*., Virus-specific cytotoxic CD4$^+$ T cells for the treatment of EBV-related tumors. *J. Immunol.* **184**, 5895–5902 (2010). doi: 10.4049/jimmunol.0902850; pmid: 20385879
81. M. F. Alvis Brazma, R. Guigo, T. Keane, A. Navarro, H. Parkinson, J. Rambla, RNA sequencing of primary B-cells infected with EBV virus, version 1, European Genome-Phenome Archive (2023); https://ega-archive.org/studies/EGAS00001007187.
82. M. F. Alvis Brazma, R. Guigo, T. Keane, A. Navarro, H. Parkinson, J. Rambla, EBNA2 ChIP-Re-ChIP in primary B-cells infected with EBV virus, version 1, European Genome-Phenome Archive (2023); https://ega-archive.org/studies/EGAS00001007626.
83. G. R. Bantug, MTBLS2243: A metabolic dependency of EBV can be targeted to hinder B cell transformation, MetaboLights (2024); https://www.ebi.ac.uk/metabolights/MTBLS2243.
84. F. Trulsson, Volcano and Heatmap generation from Transcriptome data 2 days post infection, version 1, GitHub (2024); https://doi.org/10.5281/zenodo.10854112.

ACKNOWLEDGMENTS

We thank B. Kempkes for providing EBV strains and cell lines and D. Nadal for help with preparatory work to establish efficient B cell infection. We thank R. Belle for help with establishing an infection protocol and the h.i. EBV control system. We thank all blood donors and the Blood Donation Centre of the University Hospital of Basel and the flow cytometry facility of the Department of Biomedicine at the University of Basel and University Hospital of Basel. Figures 1A and 4, E and H, were created with BioRender.com. **Funding:** Goldschmidt-Jacobson Foundation grant 2019 (B.M.-D.); University of Basel Research Fund Junior Researchers 2017 (B.M.-D.); Swiss Cancer League grant KFS-4729-02-2019 (C.H. and G.R.B.); Swiss Cancer League grant KFS-3773-08-2015 (C.H. and G.R.B.); Swiss Cancer League grant KFS-4962-02-2020 (C.Mü.). **Author contributions:** B.M.-D. conceived of, coordinated, performed, and supervised experiments and wrote the manuscript. J.J. conceived of, performed, and analyzed experiments. C.E. and P.S. performed all in vivo experiments in NSG mice and analyzed data. S.A., Y.S., C.Ma., G.U., S.R., R.S., J.E.-H., J.W., L.T., L.D., D.P., S.S., and N.K. performed and analyzed experiments. E.X. performed mouse experiments and analyzed data. N.A. established tracing experiments and analyzed data. U.D. established mass spectrometry protocols, performed experiments, and analyzed data. F.T., R.I., and M.G. performed bioinformatics analyses. T.A. and C.B. helped with patient selection from the STCS. D.K. performed AlphaFold modeling. P.D. helped with data analysis and interpretation and microscopy. J.M. helped with EBNA2 overexpression. J.L. helped establish mass spectrometry protocols and advised on experimental design. S.D. performed immunopathology experiments and helped interpret data. C.Mü. established the humanized mouse model, advised on in vivo experiments, and analyzed data. G.R.B. conceived of experiments, assisted with data interpretation, and provided technical advice. C.H. conceived of, supervised, and coordinated the research and wrote the manuscript. **Competing interests:** C.H., B.M.-D., and G.R.B. are inventors on a patent relating to this study filed by University of Basel (EP 21161105.8), which is being developed in a start-up company (Hornet Therapeutics Ltd.; scientific founder: C.H.). D.K. is a cofounder of Hornet Therapeutics Ltd. C.H. and D.K. have an indirect affiliation with Kyowa Kirin Co. Ltd. The other authors declare that they have no other competing interests. **Data and materials availability:** All data needed to evaluate the conclusions in the paper are present in the paper or the supplementary materials. Transcriptome and chromatin immunoprecipitation sequencing (ChIP-seq) data are publicly available in the European Genome-Phenome Archive (EGA) (*81*, *82*) under accession numbers EGAS00001007187 (RNA-seq) and EGAS00001007626 (ChIP-seq). Metabolome data are available in the MetaboLights database under study number MTBLS2243 (*83*). The R code used for Deseq analysis is available on GitHub (*84*). The IDO1-inhibitor KHK2455 is available from Kaori Shima (kaori.shima@kyowakirin.com) under a material transfer agreement with Kyowa Kirin Co. Ltd. **License information:**

Swiss Transplant Cohort Study (STCS) major contributors
Christoph Berger[7] and Christoph Hess[1,5]

Swiss Transplant Cohort Study (STCS) collaborators
Michael Koller[14,15], Simona Rossi[14,15], Susanne Stampf[14,15], Nicolas J. Müller[15]

[1]Immunobiology Laboratory, Department of Biomedicine, University of Basel and University Hospital of Basel, Basel, Switzerland. [5]Cambridge Institute of Therapeutic Immunology and Infectious Disease (CITIID), Department of Medicine, University of Cambridge, Cambridge, UK. [7]Experimental Infectious Diseases and Cancer Research, University Children's Hospital of Zürich, Zürich, Switzerland. [14]Data Center of Swiss Transplant Cohort Study (STCS), University Hospital Basel, Basel, Switzerland. [15]Division of Infectious Diseases and Hospital Epidemiology, University Hospital Zürich, Zürich, Switzerland.

SUPPLEMENTARY MATERIALS

science.org/doi/10.1126/science.adk4898
Materials and Methods
Figs. S1 to S12
Tables S1 to S6
References
MDAR Reproducibility Checklist
Movie S1

Submitted 25 August 2023; accepted 3 May 2024
Published online 23 May 2024
10.1126/science.adk4898